

AD-A158 253

FUSION WELDING RESEARCH(U) MASSACHUSETTS INST OF TECH
CAMBRIDGE DEPT OF MATERIALS SCIENCE AND ENGINEERING

1/1

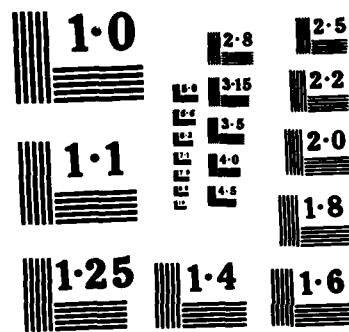
T W EAGAR ET AL. 30 APR 85 N00014-80-C-0384

UNCLASSIFIED

F/G 13/8

NL

END
FILED
GHC



NATIONAL BUREAU OF STANDARDS
MICROCOPY RESOLUTION TEST CHART

AD-A158 253

DTIC FILE COPY

SECURITY CLASSIFICATION OF THIS PAGE (When Data Entered)

(2)

REPORT DOCUMENTATION PAGE		READ INSTRUCTIONS BEFORE COMPLETING FORM
1. REPORT NUMBER	2. GOVT ACCESSION NO.	3. RECIPIENT'S CATALOG NUMBER
4. TITLE (and Subtitle) Fusion Welding Research		5. TYPE OF REPORT & PERIOD COVERED 5th Annual Technical Report April 30, 1985
7. AUTHOR(s) T. W. Eagar, G. B. Hunter, C.D. Allemand A. Block-Bolten, G. J. Dunn, D. E. Ries, R. Schoeder, K.T. Ulrich, J.L. LaPointe, A. O. Oladipupo, C.D. Sorensen, M. L. Lin		8. CONTRACT OR GRANT NUMBER(s) N00014-80-C-0384
9. PERFORMING ORGANIZATION NAME AND ADDRESS Department of Materials Science and Engineering Massachusetts Institute of Technology Cambridge, MA 02139		10. PROGRAM ELEMENT, PROJECT, TASK AREA & WORK UNIT NUMBERS
11. CONTROLLING OFFICE NAME AND ADDRESS Dr. Bruce A. MacDonald Office of Naval Research 800 N. Quincy, Arlington, VA 22217		12. REPORT DATE April 30, 1985
14. MONITORING AGENCY NAME & ADDRESS (if different from Controlling Office)		13. NUMBER OF PAGES 38
		15. SECURITY CLASS. (of this report) Unclassified
		16. DECLASSIFICATION/DOWNGRADING SCHEDULE
16. DISTRIBUTION STATEMENT (of this Report) Reproduction in whole or in part is permitted for any purposes of the United States Government. Distribution of this document is unlimited.		
17. DISTRIBUTION STATEMENT (of the abstract entered in Block 20, if different from Report)		
18. SUPPLEMENTARY NOTES		
19. KEY WORDS (Continue on reverse side if necessary and identify by block number)		
20. ABSTRACT (Continue on reverse side if necessary and identify by block number) This report summarizes progress during the fifth year of fundamental research on welding processes. Studies include metal vapors in the arc, development of a high speed infrared temperature monitor, digital signal analysis as a weld process monitor, convection in arc weld pools, droplet transfer and contact tip wear in gas metal arc welding of titanium, and fracture toughness of HY-80 weldments.		

DD FORM 1 JAN 73 1473

EDITION OF 1 NOV 65 IS OBSOLETE
S/N 0102-014-66011

SECURITY CLASSIFICATION OF THIS PAGE (When Data Entered)

DTIC
ELECTED
S AUG 21 1985
D
E

FUSION WELDING RESEARCH

by

T. W. Eagar, G. B. Hunter, C. D. Allemand
A. Block-Bolten, G. J. Dunn, D. E. Ries, R. Schoeder,
K. T. Ulrich, J. L. LaPointe, A. O. Oladipupo, C. D. Sorensen, M. L. Lin

Fifth Annual Technical Report
Contract N00014-80-C-0384
to
Office of Naval Research
Department of the Navy
Arlington, VA 22217

Attention: Dr. Bruce A. MacDonald

April 30, 1985

Accession For	
NTIS GRA&I	<input checked="" type="checkbox"/>
DTIC TAB	<input type="checkbox"/>
Unannounced	<input type="checkbox"/>
Justification	
By _____	
Distribution/ _____	
Availability Codes	
Dist	Avail and/or Special
A-1	



Reproduction in whole or in part is permitted for any purposes of the
United States Government. Distribution of this document is unlimited.

85 822 017

Table of Contents

	<u>Page</u>
ABSTRACT	3
I. INTRODUCTION	4
II. SPECTROSCOPY OF ARC WELDING	5
A. Metal Vapors in the Arc	5
B. Temperature Measurements of the Weld Pool	5
III. WELDING OF HEAVY SECTION TITANIUM	6
A. Droplet Transfer in Gas Metal Arc Welding	6
B. Contact Tip Wear in Gas Metal Arc Welding	6
IV. FRACTURE TOUGHNESS OF HY-80 WELDMENTS	7
V. AUTOMATION OF ARC WELDING	7
A. Signal Analysis as a Weld Process Mointor	7
B. Convection in Arc Weld Pools	9
SUMMARY	10
REFERENCES	11
APPENDICES	
A. "Metal Vaporization from Weld Pools" by A. Block-Bolten and T. W. Eagar.	12
B. "Metal Vapors in Gas Tungsten Welding Arcs" by G. J. Dunn (abstract).	17
C. "Characteration of Molten Weld Pool" by J. Szekely, T. W. Eagar, J. McKelliget, and G. Dunn (abstract).	18
D. "Spectrometric Temperature Measurements of Thermal Radiators" by G. B. Hunter (abstract).	19
E. "An Improved Method of Multi-wavelength Pyrometry: by G. B. Hunter	20
F. "A method of Filming Metal Transfer in Welding Arcs" by C. D. Allemand, R. Schoeder, D. E. Ries, and T. W. Eagar	27
G. "Wear of Contact Tips in Gas-Metal Arc Welding of Titanium" by J. L. LaPointe (abstract).	30
H. "Contact Tip Wear in Gas-Metal Arc Welding of Titanium" by K. T. Ulrich, J. L. LaPointe, G. B. Hunter, and T. W. Eagar (abstract).	31
I. "Influence of Arc Pressure on Weld Pool Geometry" by M. L. Lin and T. W. Eagar	32

ABSTRACT

↳ This report summarizes progress ⁽ⁱⁿ⁾ during the fifth year of fundamental research on welding processes. Studies include: metal vapors in the arc; development of a high speed infrared temperature monitor; digital signal analysis as a weld process monitor; convection in arc weld pools; droplet transfer and contact tip wear in gas metal arc welding of titanium; and fracture toughness of HY-80 weldments. Key words: → (to j, v)

I. INTRODUCTION

This report describes work performed in the MIT Welding Laboratory under Office of Naval Research sponsorship. The work is generally fundamental in nature, but attempts have been made to interface the studies with specific U.S. Navy Programs. The best examples of the directed programs include the evaluation of the fracture toughness of HY-80 weld metal and the study of contact tip wear in titanium welding.

The research conducted from 15 February 1983 to 15 February 1984 can broadly be divided into four main topics, viz.;

1. Spectroscopy of arc welding
2. Welding of heavy section titanium
3. Fracture toughness of HY-80 weld metal
4. Automation of arc welding automation

A

II. SPECTROSCOPY OF ARC WELDING

Spectroscopic studies of the arc welding process performed during the past contract year include development of a Multichannel Infrared-Red Temperature Micro-Analyzer, and a study of light emissions from the arc. These two studies are coupled through a thermodynamic upper-bound analysis which has been published previously (1), and was expanded in a recently published paper (Appendix A).

A. Metal Vapors in the Arc

Metal vapors in gas tungsten welding arcs are being studied in order to determine the effects of these vapors on arc properties, and subsequently, on weld bead configuration. Emission spectroscopy and monochromatic photography were used to determine the composition and distribution of vapors in the arc.

This project has produced one thesis, the abstract for which is included in Appendix B. Two papers are now being prepared for publication based on this work. Some results for this project were also presented at an AIME conference. The abstract for this presentation is included in Appendix C. Another sponsor (U.S. D.O.E.) has funded a continuation of this work into an examination of light emissions from the arc as a weld process sensor.

B. Temperature Measurements of the Weld Pool

In order to experimentally confirm theories on weld pool convection and vaporization cooling, this project is an attempt to produce absolute temperature distribution maps of the weld pool surface. A unique radiation pyrometric technique is being developed to make these measurements using a Multichannel Infrared-Red Temperature Micro-Analyzer (MIRTMA) prototype device.

This work has produced one thesis, the abstract for which is included in Appendix C, and one technical paper (Appendix DOE) presented at a SPEI conference. Another paper has been accepted for publication and one or two more are now being prepared.

Research in this area is now continuing in order to refine the temperature measurement technique and develop an improved MIRTMA device. It is predicted that this measurement technique will have applications beyond the welding field.

III. WELDING OF HEAVY SECTION TITANIUM

Joining of heavy section titanium is of particular concern to the Navy for advanced systems.

A. Droplet Transfer in Gas Metal Arc Welding

This project has been postponed for this contract period to fund other projects and until an interested student could be found. It is expected that this research will be restarted during the next contract year. During the past year, one paper has been published (Appendix E).

B. Contact Tip Wear in Gas Metal Arc Welding

Copper contact tips wear very rapidly when titanium electrodes are used in gas metal arc welding. The goal of this work was to identify the mechanisms causing the increased wear and to find methods to reduce the wear. During the past year, this project has produced one thesis and was presented at an AIME conference, the abstracts for which are in Appendices F and G, respectively. This project has been discontinued.

IV. FRACTURE TOUGHNESS OF HY-80 WELDMENTS

HY-80 is an important alloy for a variety of Navy systems. The fracture toughness of thick plate submerged arc welds is of particular interest. This project is an investigation into the metallurgical factors influencing charpy energy of these weldments.

Work on this project was completed at the beginning of this last contract year. One technical paper on this research is now being prepared for publication.

V. AUTOMATION OF ARC WELDING

Automation is one area of welding technology that promises to pay tremendous dividends if high sensitivity, rugged sensors can be developed. One possible sensor is the arc itself, which is known to respond to geometric and chemical discontinuities at frequencies up to 20 kHz . In one study, digital signal analysis is being used to measure these responses. In a second effort, the effect of convection on weld pool shape and defect formation is being studied. This latter topic is of great importance in developing processes capable of producing weld pools of desired size and quality.

A. Signal Analysis as a Weld Process Monitor

One of the difficulties associated with automation of arc welding processes is the lack of a reliable in-process weld quality sensor. The intense heat, light, and electric fields in the vicinity of the arc form a hostile environment to nearly all sensors. By using the arc itself as a sensor, this difficulty is overcome. The purpose of this research project is to develop a weld quality sensor based on the electrical properties of

the welding arc. Digital signal processing of the arc voltage and current is an effective means of determining these properties. During previous contract periods, the hardware and software necessary to acquire and analyze the signals has been developed. Preliminary studies have shown the optimum current waveform. During the present contract period, actual measurements of weld properties have been obtained.

In order to study the electrical properties of the arc, experiments are performed with welding current regulated to within 1% of the selected value and a constant arc length. The current is considered to be the input to the arc/puddle system and the arc voltage is considered to be the output. These voltage and current signals are analyzed to determine the frequency response function of the arc puddle system and the electrical properties of the arc are determined by calculating the current-voltage transfer function of the system (2).

The experimental work performed during the past year can be classified into two groups. The first group consists of experiments designed to show the effects of weld defects on the electrical properties of the arc, and the second consists of experiments designed to study the dynamics of the weld pool. The current waveform and sampling parameters have been optimized during the experimental program to improve the signal-noise ratio of the system gain function. Thus, the quality of the received signals is now very high, providing a high degree of confidence in the results. Although the sensitivity of the technique remains to be assessed, the capability to measure puddle oscillations has been demonstrated.

A limited ability of this analysis technique to detect changes in weld chemistry, weld geometry, and weld size has been shown. Work is continuing

in an effort to identify the limits of sensitivity and practicality of this technique as a means of sensing weld quality. A thesis on this topic and one or two papers will be completed in the next contract year.

B. Convection in Arc Weld Pools

Recent work by many investigators is emphasizing the importance of fluid convection on arc weld pool geometry. Related work supported by the U.S. D.O.E. in this laboratory resulted in a technical paper which recently won an AWS award (3).

Work on this project has concentrated mainly in the high current range (250-500A). At these currents, a deep, surface depression is formed which can be explained by a rapid vortex flow in the pool. This theory has been explained in a previously published paper (4).

One technical paper is scheduled to be published soon on arc force measurements (Appendix H) in support of this work. This paper presents arc force measurements up to 600A as an extension of a previously published technical note (5). A Thesis on the entire project will be completed in the next contract year, and one or two additional papers are being prepared. This project will be continued.

SUMMARY

During the past year, significant progress has been made in many areas of this project. The research conducted over this time involved spectroscopy of arc welding, welding of heavy section titanium, fracture toughness of HY-80 weldments, and automation of arc welding.

REFERENCES

1. A. Block-Bolten and T. W. Eagar, "Selective Evaporation of Metals from Weld Pools", in Trends in Welding Research in the United States, ASM, Metals Park, OH, 53-62, 1982
2. J. S. Bendat and A. G. Piersal, Engineering Applications of Correlation and Spectral Analysis, Wiley and Sons, New York, NY, 1980.
3. G. M. Oreper, T. W. Eagar, and J. Szekely, "Convection in Arc Weld Pools", Welding J., 62 (11), 3075-3125, 1983.
4. M. L. Lin and T. W. Eagar, "Influence of Surface Depression and Convection on Arc Weld Pool Geometry", in Transport Phenomena in Materials Processing, PED - Vol. 10/HTD-Vol. 29, M. M. Chen, J. Mazumder, and C. L. Tucker III, eds., ASME, New York, NY, 63-72, 1983.
5. T. D. Burleigh and T. W. Eagar, "Measurement of the Forced Exerted by a Welding Arc", Metall. Trans., 14A (6), 1223-1224, 1983.

A. BLOCK-BOLSEN and T. W. EAGAR

Experimental studies of alloy vaporization from aluminum and stainless steel weld pools have been made in order to test a vaporization model based on thermodynamic data and the kinetic theory of gases. It is shown that the model can correctly predict the dominant metal vapors that form but that the absolute rate of vaporization is not known due to insufficient knowledge of the surface temperature distribution and subsequent condensation of the vapor in the cooler regions of the metal. Values of the net evaporation rates for different alloys have been measured and are found to vary by two orders of magnitude. Estimated maximum weld pool temperatures based upon the model are in good agreement with previous experimental measurements of electron beam welds.

I. INTRODUCTION

LOSS of alloying elements from the weld pool due to vaporization is important for a number of reasons. Firstly, if the loss is great enough, the mechanical properties of the weld may be impaired.¹ Secondly, the composition of a welding arc plasma influences the temperature of the arc,² arc stability, and fume formation.³ Thirdly, it has been shown that vaporization places an upper limit on the temperature produced on the surface of the metal due to evaporative cooling.^{4,5}

A previous paper has presented a formalism for calculation of partial pressures of metal vapors above steel weld pools.⁶ This analysis provided an estimate of the power lost by evaporation as well as an upper bound on the surface temperature of steel weld pools as a function of alloy composition. In the present paper, this analysis is extended to evaporation from aluminum and copper alloy weld pools where different metal vapors dominate. The results of the calculations are then compared with experimental results from both aluminum and steel weld metals.

II. EXPERIMENTAL PROCEDURE

Both steel samples and aluminum alloy samples were subjected to extended time welding in a specially adapted chamber which was coupled to a direct reading emission spectrometer. The chamber was supplied with a lens guiding the light to the spectrometer grating. A mirror imaging device was provided to ensure uniform position of the work and the electrode. The hearth was water cooled and the entire system was purged with argon flow. The rotating water-cooled copper hearth shown in Figure 1 was employed in the case of 12.5 cm diameter 304 steel samples, but the rotation has not proven useful. The slight deviations of the rotating sample cause periodic sinusoidal changes in the arc length and corresponding oscillations in the spectral signal. Therefore, this experiment could be characterized only by lower and upper limits of spectrographic signal, voltage, current, and final weld chemical composition, and not by a uniquely defined value of each of those parameters. As a result, the experimental data presented in this paper

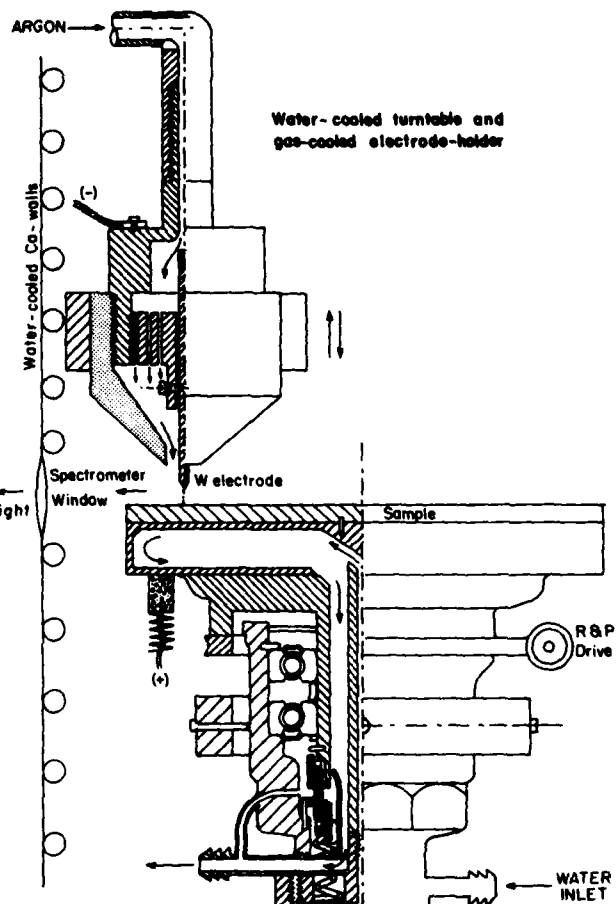


Fig. 1—Water-cooled turntable and gas-cooled electrode holder.

were obtained from stationary arc welds where the arc length was more controllable.

The 0.35 to 1.10 g steel samples consisted of 1.6 mm diameter wires (502, 505, 5151, and 5212 steels) or 1.1 mm wire (410 steel) or 2.4 mm diameter wires (308L and 309L steels). The thoriated tungsten electrodes of 1.6 mm diameter were mounted as shown in Figure 1. Each steel sample was weighed before and after each experiment, yet only the 308L and 309L stainless steel samples gave reasonable weight loss results (Figure 2), as other steels were too readily oxidized in spite of the welding grade argon environment. The small amount of impurities in this gas stream and the extended time of these tests created a significant weight

A. BLOCK-BOLSEN, Research Scientist, is now with the Department of Metallurgy and Materials Science, University of Toronto. T. W. EAGAR, Associate Professor, Materials Engineering, is with the Department of Materials Science and Engineering, Massachusetts Institute of Technology, Cambridge, MA 02139.

Manuscript submitted September 23, 1983.

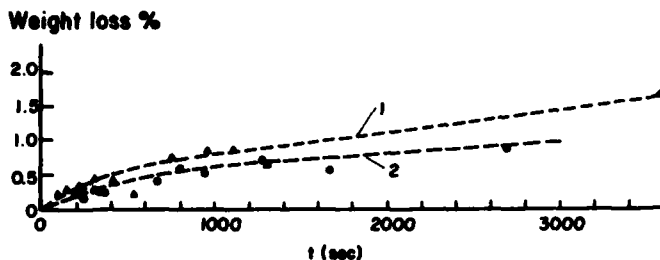


Fig. 2—Weight-loss experiment. 1—weight loss curve for 308L stainless steel, 2—for 309L stainless steel; average voltage 11 V, current set at 15 A; average sample size 1 g.

loss or gain by oxidation over the course of the experiment in these other steels. The compositions of the steel and Al-alloy samples used are given in Table I. The sizes of the Al-alloy samples are specified in the caption of Figure 8.

Atomic absorption chemical analysis was performed on buttons from the melted steel wires and on shavings drilled out of craters of the Al-alloy samples after melting.

The spectrographic signals were ratioed relative to the most abundant element of the alloy: Fe in steels and Al in Al-alloys, through a system of analog dividers. The spectrographic signals from the photomultipliers were measured by Keithley Model 480 picoamperometers.

III. PREDICTION OF VAPORIZATION TENDENCY

As shown in a previous paper,⁵ the logarithm of the partial pressure of an alloy component in the gas phase is proportional to the sum of the logarithms of the standard pressure of the pure element and the activity of the element in the alloy, i.e.,

$$\log \bar{p}_A = \log p_A^0 + \log a_A \quad [1]$$

where

\bar{p}_A is the partial pressure of element A in the gas phase, p_A^0 is the standard pressure of pure A, and a_A is the activity of A in the alloy.

The vaporization rate can be predicted from the kinetic theory of gases,⁶

$$r_A = 44.331 \bar{p}_A \left(\frac{M_A}{T} \right)^{1/2} [\text{g} \cdot \text{s}^{-1} \cdot \text{cm}^{-2}] \quad [2]$$

where

r_A is the rate of evaporation of element A, M_A is the molecular weight of A,

T is the absolute temperature, and \bar{p}_A has units of atmospheres.

The evaporation power loss P_L is then

$$P_L = r_A (L_A - \Delta H_A) [\text{watt} \cdot \text{cm}^{-2}] \quad [3]$$

where

L_A is the heat of evaporation of pure A and

ΔH_A is the partial molar heat of mixing of A in the alloy.

The evaporative energy loss, E_L , is

$$E_L = r_A (L_A - \Delta H_A) t [\text{watt} \cdot \text{cm}^{-2} \cdot \text{s}], \quad [4]$$

where t is time. In most cases ΔH_A is small compared to the heat of evaporation. If the element of interest is the solvent such as iron in steel or aluminum in aluminum alloys, ΔH_A can be neglected.

Using Eq. [1], it is possible to construct pressure-temperature diagrams for aluminum, copper, and iron base alloys as shown in Figures 3, 4, and 5. These diagrams

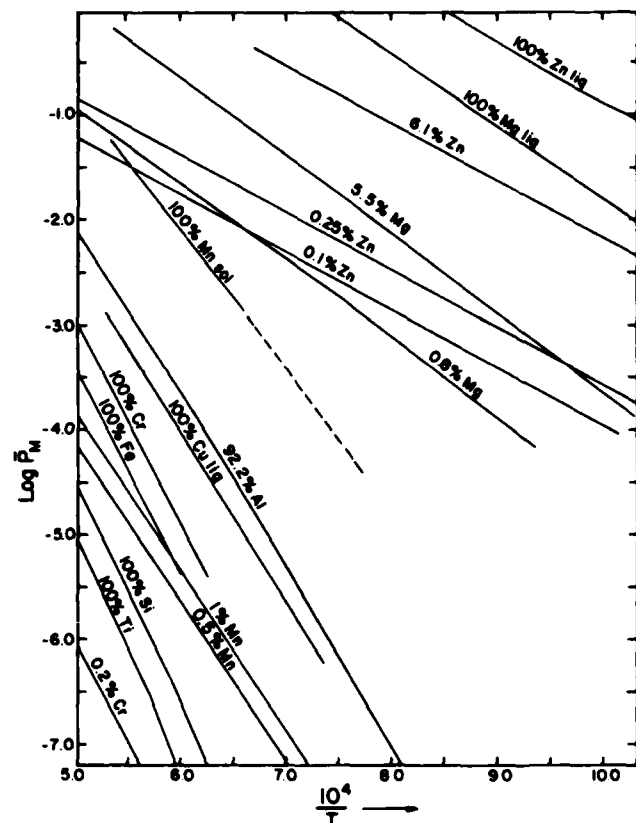


Fig. 3—Aluminum alloys: vapor pressures for some constituent alloy additions.

Table I. Compositions of Starting Materials Used in This Study

Steels: Compositions As Delivered				Al Alloys: Composition As Delivered		
Steel Number	Pct Fe	Pct Mn	Pct Cr	Alloy Number	Pct Zn	Pct Mg
410	86.70	0.45	12.03	7075	5.82	2.30
502	94.87	0.45	4.00	5083	0.014	4.06
505	89.70	0.45	9.06	5456	0.019	5.20
5151	98.05	0.54	0.99/1.37	6061	0.063	0.95
5212	97.30	0.55	1.91	2024	0.058	1.46
308L	67.25	1.91	21.00	1100	<0.010	<0.010
309L	59.65	1.79	26.08			
304	68.80	1.75	18.66			

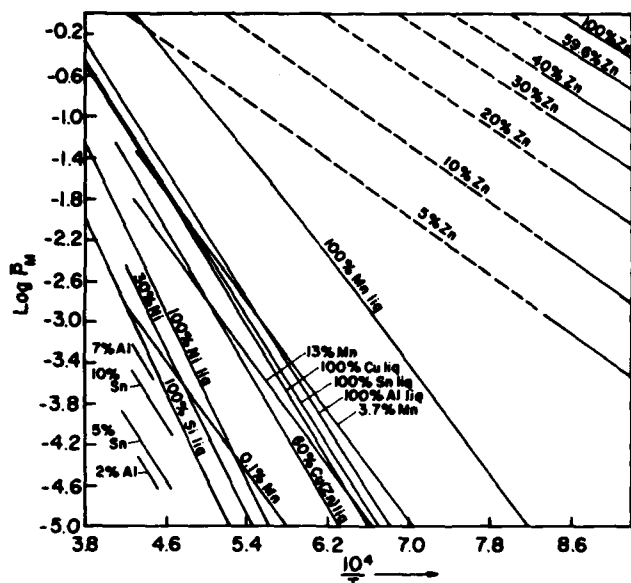


Fig. 4—Copper alloys: vapor pressures for some constituent alloy additions.

are based on tabulated values of activity coefficients.¹² To extrapolate Hultgren's activity (a_0) data to other (a_n) temperatures, $\log a_n = \log a_0 + \frac{\Delta\bar{G}^{\circ}}{RT} (T_0 - T_n) / 4.575 T_0 T_n$, $\Delta\bar{G}^{\circ}$ was assumed identical to $\Delta\bar{H}$, and $\Delta\bar{G}^{\circ}$ or $\Delta\bar{H}$ was used, whichever was available. $\Delta\bar{G}^{\circ}$ is partial excess free energy of mixing.

As shown previously, mild interaction effects between the alloying elements in ternary and higher order systems can often be neglected;⁵ however, strong interactions where compounds tend to form in the liquid metal cannot be neglected.

As shown previously for steels,⁵ Eq. [4] can be combined with the arc surface energy distributions of Nestor⁷ to produce upper limits on the surface temperature of the weld pool. Figure 6 shows such an upper bound analysis for a number of aluminum alloys. The upper bound analysis assumes that all of the power input to the weld pool is lost by vaporization of the metal. Since this is clearly not true, a least upper bound on the temperature of the weld pool surface can be obtained if one knows what fraction of the total input power is lost by evaporation. As will be shown later, it is difficult to measure this quantity with precision. The concept of the upper bound temperature of the pool is outlined in a previous paper.⁵

IV. CORRELATION OF THEORY WITH EXPERIMENT

As noted in the experimental procedure section, a number of steel and aluminum alloys were arc melted for unusually long times in order to evaporate enough alloying components to be detectable by chemical analysis. Due to problems of oxidation, only two of the stainless steel samples gave consistent results. The Mn and Fe spectrographic signals normalized to the relatively stable Cr signals as a

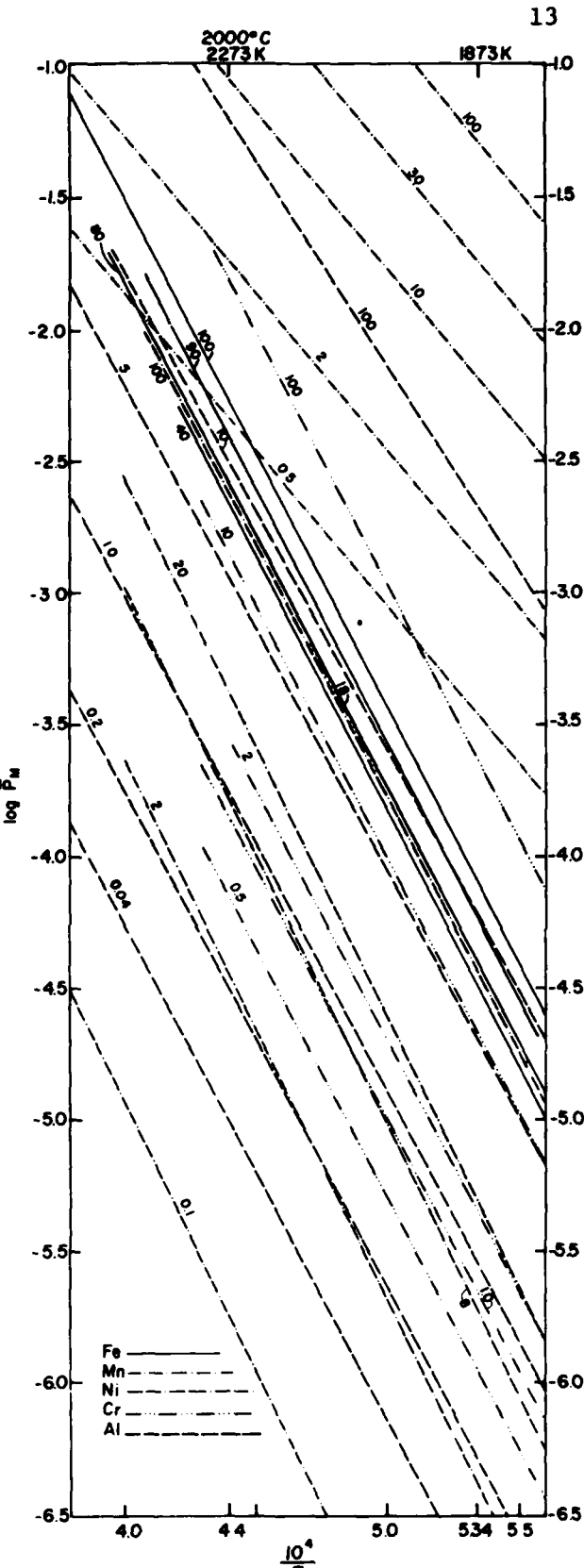


Fig. 5—Steels: vapor pressures for some constituent alloy additions. Numbers on curves represent weight percentages.

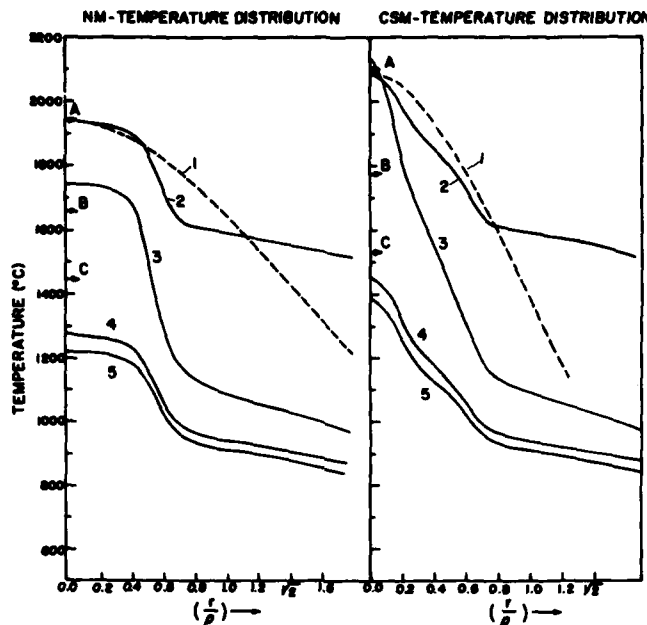


Fig. 6—Normal mode and cathode spot mode temperature distributions for the 5456 Al-alloy. The temperature is plotted vs non-dimensional distance r/ρ from the center of the arc; ρ is defined as in Ref. 5 as $\rho = \sqrt{V/2\pi C}$ where V is the total power of the arc (in watts) and C is the peak power density in watt \cdot cm $^{-2}$. The plots are based on Fig. 3 and on Nestor's power distribution curves. Should 100 pct of energy go into evaporation of pure aluminum, point A on temperature ordinate would correspond to the expected maximum temperature of the weld pool. Points B and C mark 10 pct and 1 pct energy going into evaporation, respectively. Curves 1 are normal distribution (of energy) curves for pure aluminum. Curves 2 are those based on Nestor for pure Al. Curves 3 are for evaporation of 0.25 pct Zn in Al, and curves 4 and 5 are for evaporation of 4.7 pct Mg in Al and 5.5 pct Mg in Al, respectively.

function of arc melting time are shown in Figure 7. It will be noted that Mn is the primary element lost as predicted by Figure 5.

In order to test the model more completely, a series of six aluminum alloys with varying zinc and magnesium contents were selected. Aluminum alloys were selected because the Zn and Mg have very high vapor pressures as compared to aluminum; and as seen in Figure 6, this significantly lowers the upper bound temperature.

The aluminum alloys can be separated into four groups, where

- I Zn vapor dominates,
- II Mg vapor dominates,
- III nearly equivalent Zn and Mg vapor pressure exists,
- IV Al vapor dominates.

Alloy 7075 belongs in group I as seen in Figure 8. If we compare Table II and Figure 3, we see that the high zinc concentration in 7075 alloy places the zinc isopleth of Figure 2 well above the Mg isopleth for this alloy.

Alloys 5083 and 5456 belong to group II as seen in Figures 9 and 10. This is again consistent with the predictions made from Table II and Figure 3.

Alloys 6061 and 2024 belong to group III as shown in Figures 11 and 12, respectively. This result is not as easily predicted from Figure 3 since the exact composition of the alloy and the temperature of the weld pool surface are not known precisely. Nonetheless, the spectrographic data of Figure 13 clearly show a simultaneous rise in the spectral signals for both Mg and Zn. It is interesting to note that Zn typically reaches its maximum presence in the vapor later than Mg, probably due to kinetic limitations since Zn is more dilute in the alloy. The gradual rise of both elements

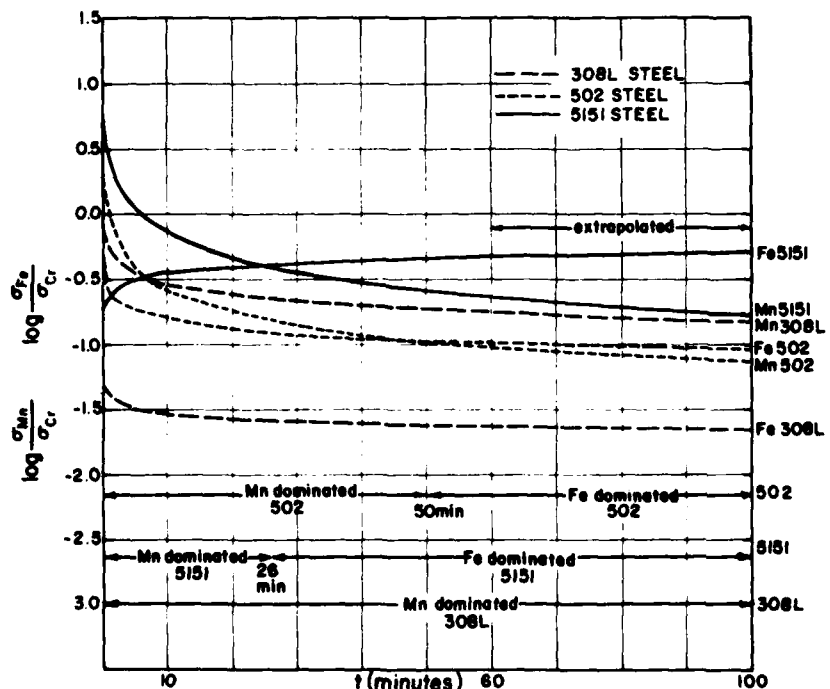


Fig. 7—Decay of normalized signal ratios of iron to chromium and manganese to chromium (Cr content does not change significantly) for three different steels. As can be seen, Mn dominates over the iron in the vapor phase. Only after long periods of time does iron start to dominate in the 5151 and 502 steels.

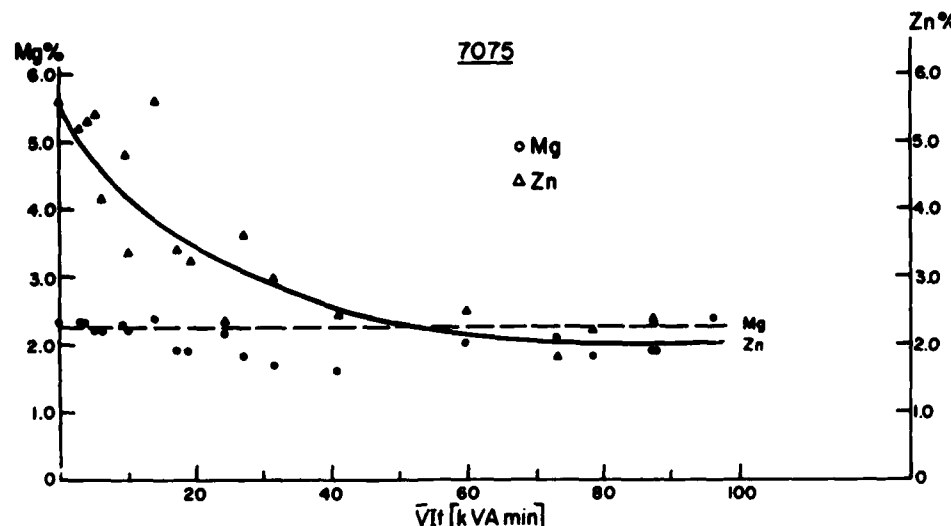


Fig. 8—Loss of Zn vs energy input in [kVA min] from aluminum alloy 7075. No change in Mg was found. Original contents of Mg and Zn were 2.3 pct and 5.6 pct, respectively. The voltage during tests varied between 12.5 and 15 V; current was set between 125 A and 150 A; the longest experiment lasted 45 min. The size of the samples was 52 × 51 × 12.7 mm. Rates of evaporation for this and other alloys are given in Table III.

Table II. Calculated Center Line Surface Temperature of Weld Pools for Six Aluminum Alloys

1100 Alloy, 0 to 0.1* Pct Zn, Bal. Al			2024 Alloy, 0.25 Pct Zn; 1.2 to 1.8* Pct Mg			5083 Alloy, 0.25 Pct Zn; 4 to 4.9* Pct Mg		
Power Density, Pct	Vapor Domination	t °C Range NM/CSM	Power Density, Pct	Vapor Domination	t °C Range NM/CSM	Power Density, Pct	Vapor Domination	t °C Range NM/CSM
100	Al	1935*/2091	100	Mg	1422*/1751	100	Mg	1268*/1491
10	Zn*, Al	1364*/1614	10	Mg	1101*/1290	10	Mg	994*/1126
1	Zn*, Al	968*/1530	1	Zn, Mg* ^{CSM}	870*/ 975	1	Mg	807*/ 905
5456 Alloy, 0.25 Pct Zn; 4.7 to 5.5* Pct Mg			6061 Alloy, 0.25 Pct Zn; 0.8 to 1.2* Pct Mg			7075 Alloy, 5.1 to 6.1* Pct Zn; 2.1 to 2.9 Pct Mg		
Power Density, Pct	Vapor Domination	t °C Range NM/CSM	Power Density, Pct	Vapor Domination	t °C Range NM/CSM	Power Density, Pct	Vapor Domination	t °C Range NM/CSM
100	Mg	1220*/1451	100	Mg	1513*/1882	100	Zn	1057*/1242
10	Mg	964*/1104	10	Zn, Mg*	1154*/1358	10	Zn	795*/ 909
1	Mg	783*/ 891	1	Zn	870*/ 994	1	Zn	612*/ 695

Normal Mode NM 200 A, 14.0 V, $C = 2180$ [watt · cm⁻²]
 Cathode Spot Mode CSM 200 A, 14.8 V, $C = 6120$ [watt · cm⁻²] peak power density
 *Note that the lower calculated temperatures correspond to the higher alloy compositions.

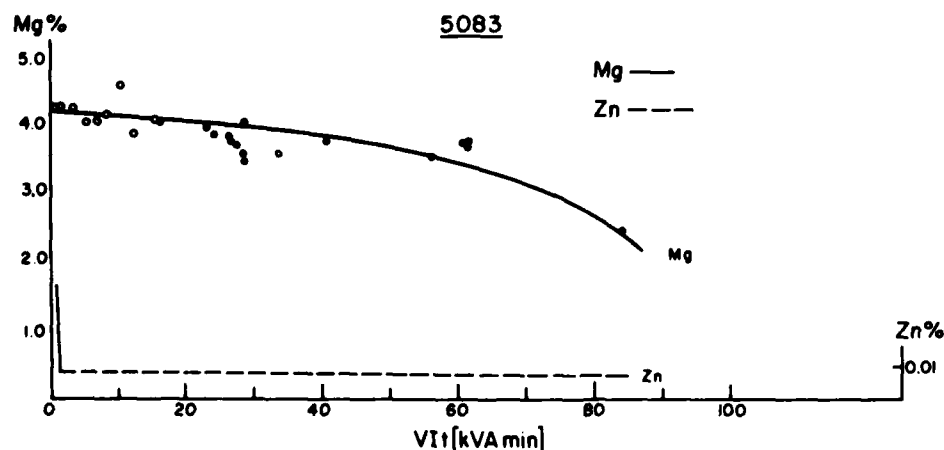


Fig. 9—Aluminum alloy 5083. Loss of Mg vs energy input. The change in Zn content occurs only in the first few seconds of the experiment, then Zn remains constant. The original Mg content was 4.3 pct. Voltage and current were 15 V and 125 A. The longest experiment lasted 45 min.

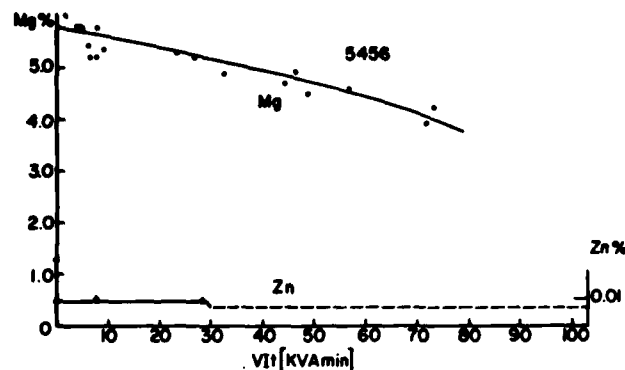


Fig. 10—Aluminum alloy 5456. Loss of Mg vs energy input. The changes in Zn content occur only in the first seconds of the experiment, then Zn remains constant. Original Mg content 5.8 pct. Average voltage was 15 V, and current was set between 125 and 150 A. The longest experiment lasted 45 min.

is most likely due to increase in the size of the weld pool with time. Alloy 1100 is the only sample tested which belongs to group IV of the series.

Summarizing, Figures 8 to 12 show the analyses taken from the weld pools of different Al-alloys during extended time welding. The 7075 alloy with Zn-vapor domination (Figure 8) exhibits changes only in Zn content, while Mg content stays constant. In Figures 9 and 10, the Mg-vapor dominated 5083 and 5456 alloys show Mg-content falling off, while Zn-content stays constant or below the detection level. Figures 11 and 12 for alloys 6061 and 2024 prove that both these alloys exhibit mixed vapor domination and both Zn and Mg contents change with time. In addition, SEM semiquantitative analyses have also shown changes in Zn only for the 7075 alloy, changes in Mg only for 5083 and 5456 alloy, and changes both in Mg and Zn content for the 2024 and 6061 alloys.

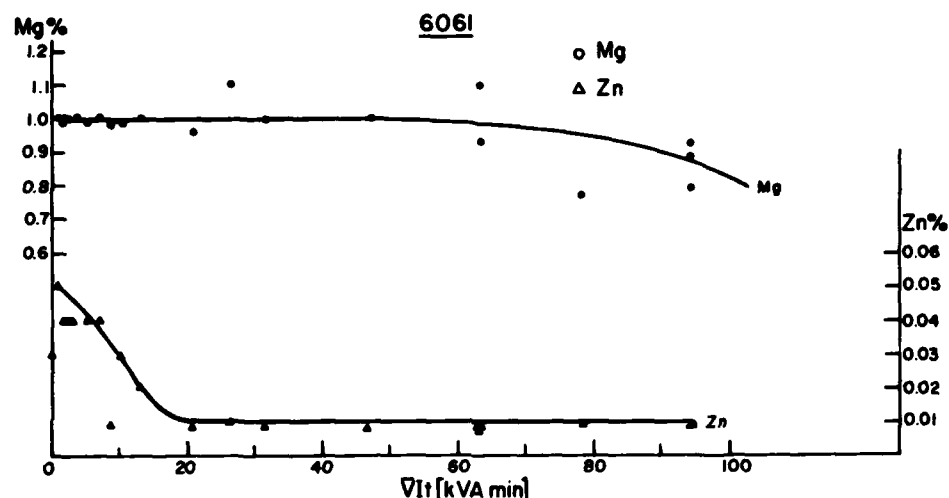


Fig. 11—Aluminum alloy 6061. Loss of Mg and Zn vs energy input. Original Mg content was 0.95 pct and the original Zn content 0.06 pct. Average voltage 14 V; the current was set at 150 A. Longest experiment lasted 45 min.

Table III. Net Energy Lost from Weld Pool by Evaporation of Alloying Elements

Group	Al-Alloy	Evaporating Element	Apparent Initial Net Evaporation Rate $[\mu\text{g s}^{-1} \text{cm}^{-2}]$	Apparent Long-Term (Mean) Evaporation Rate $[\mu\text{g s}^{-1} \text{cm}^{-2}]$	Theoretical Evaporation Energy $(L - \Delta H)^{-1} [\mu\text{g J}^{-1}]$	Apparent Evaporation per Gross Energy Input* $(\mu\text{g J}^{-1} \times 10^3)$	Percent of Arc Energy Lost by Evaporation	Source of Data (Figure No.)
I	7075	Zn	94.9	30.5	631.1	91.4	0.0144	8
		Mg	—	—	173.5	—	—	
II	5083	Zn	(11.3)	~0	631.1	38.0	0.0060	9
		Mg	5.6	12.1	173.5	40.6	0.0235	
	5456	Zn	—	~0	631.1	—	—	10
III	6061	Mg	9.7	12.7	173.5	49.0	0.0280	11
		Al**	0	(90 to 230)	92.8	—	—	
	2024	Zn	1.2	1.2	631.1	3.6	0.0006	12
		Mg	0	1.2	173.5	3.6	0.0021	
		Zn	12.0	1.3	631.1	3.8	0.0006	
		Mg	10.0	3.4	173.5	3.4	0.0020	

*gross energy input, Refs. 8, 9

**from soot formation and Al-ball growth

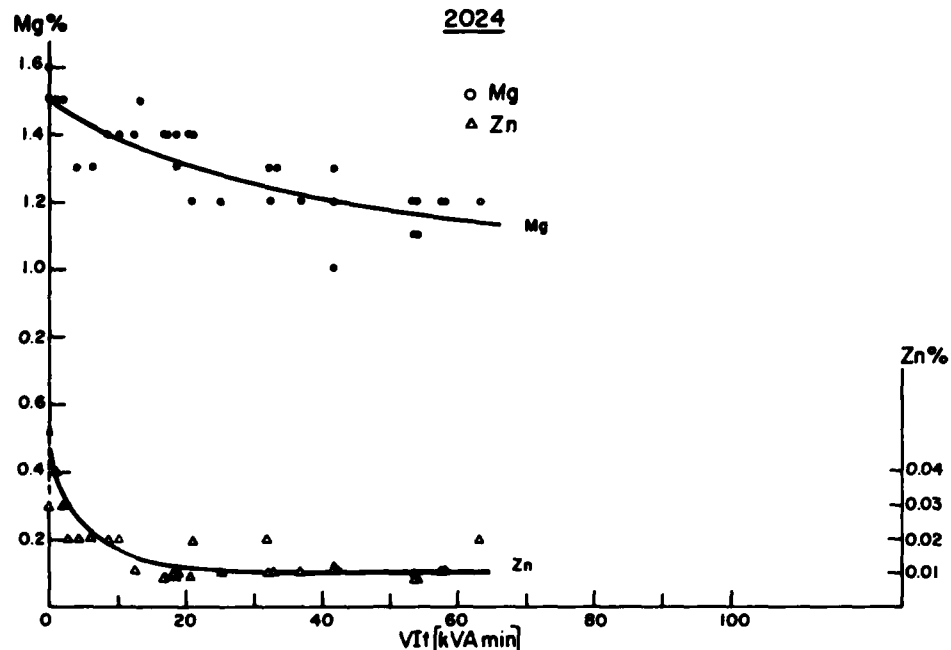


Fig. 12—Aluminum alloy 2024. Loss of Mg and Zn content vs energy input. Original Mg content 1.5 pct, Zn content 0.06 pct. Average voltage was 14 V, and the current was set at 150 A. Longest experiment lasted 30.2 min.

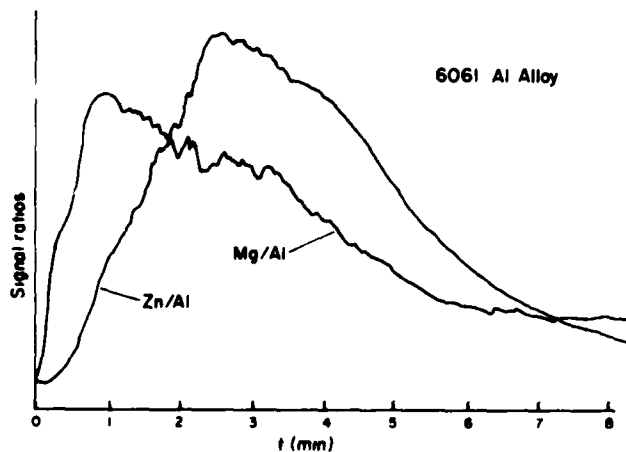


Fig. 13—Signal ratios of Mg and Zn normalized to aluminum, as typically observed for the 6061 aluminum alloy. The Mg/Al signal ratio is magnified 10 times.

From Figures 8, 9, 10, 11, and 12, values of apparent initial evaporation rate, apparent long term (mean) evaporation rate, and apparent evaporation per unit of energy have been calculated. The latter value is normalized to gross energy input^{8,9} which is half of the total arc power input, as the other half is lost to the environment and does not enter the weld pool. All these values, together with percentages (referred to theoretical evaporation per unit energy ($L - \Delta H$)⁻¹ [J⁻¹]) are displayed in Table III. It is seen that the net power lost by vaporization is much less than one percent of the total power input to the metal. As will be discussed later, this is much less than the absolute evaporative power loss; however, much of the absolute evaporative power is regained by condensation of the vapors in cooler regions of the weld pool.

V. DISCUSSION

The preceding results indicate that the model can effectively use existing thermodynamic data to predict the dominant metal vapors above the weld pool; however, it would be useful if one could predict weld pool surface temperature and hence the rate of alloy element loss. This proves to be a much more difficult task.

Quigley, *et al.*⁹ have estimated the evaporative power loss from a gas tungsten arc to be of the order of 2 pct of the total power. If this is true, it would reduce the upper bound temperatures based on 100 pct evaporative power loss as shown in Figure 6 and in Table II. Indeed, if one were to assume absolute evaporative power loss to lie between 1 and 10 pct of the total power, the surface temperature limit would drop by 200 to 500 °C for aluminum alloys. Table II shows that the surface temperature of aluminum alloy arc welds could vary from just above the melting temperature to 700 °C superheat depending on alloy composition and the amount of heat lost by vaporization.

As shown in Table III and Figures 8 through 12, weight loss measurements based on alloying element loss from the weld samples gives net evaporative losses between zero and $95[\mu\text{g} \cdot \text{s}^{-1} \cdot \text{cm}^{-2}]$. This corresponds to maximum net vaporization losses of roughly 0.015 pct of the net incident power; however, it is believed that more metal than this is vaporized from the center of the pool and then recondenses on cooler regions, thus recycling through the system. This is indirectly confirmed by spectrographic monitoring of calcium vapor in 304 stainless steels.¹⁰ The calcium spectrographic lines remain strong and do not diminish after 15 minutes of welding even though there is only 10 ppm Ca in the steel. The only way this small amount of Ca could remain after such a long time is if it is "recycled" into the metal by condensation. Although it is not possible to measure how much vapor condenses back into the pool rather

than is lost, it is believed that a larger fraction of Zn recondenses back to the pool than is lost from the system. In a sense, this is confirmed by the temperatures calculated for the 7075 alloy in Table II. If the temperature were low enough for only 0.015 pct of the power to be lost by vaporization, then the liquid would be cool enough to solidify. It is clear that at least several percent of the power at the center of the 7075 alloy pool must be lost by zinc vaporization. Much of this power is recovered at the edges of the pool as the vapor condenses. Because of this evaporation-condensation process it is very difficult to determine the absolute vaporization rate with any accuracy.

Schauer *et al.* used an infrared pyrometer to measure the weld pool surface temperature of electron beam welds in steel and aluminum.¹¹ If one assumes that the power lost from the electron beam weld pool is $6000 \text{ watts} \cdot \text{cm}^{-2}$, the measured temperatures are in reasonable agreement with the values predicted by the model presented here as seen in Table IV. Indeed, these results are perhaps the most conclusive in showing that evaporative power losses set an upper limit on the surface temperature of a weld pool. In general, these power losses probably lie between 1 and 10 pct of the total power, but the value varies somewhat with alloy content and with input power density. These losses provide a prediction of maximum arc weld pool surface temperatures between the melting point and 1600°C for aluminum alloys and between 2000°C and 2500°C for steels. The high energy density processes such as laser and electron beam can produce even higher surface temperatures with greater rates of alloy vaporization than arc welds.

VI. CONCLUSIONS

A thermodynamic model of vaporization from weld pools has been presented which can predict the dominant metal vapors that form during welding in the absence of strong compound forming elements such as oxygen or nitrogen. The evaporative power loss in arc welding lies between 1 and 10 pct of the incident power, although more precise measurement is difficult due to condensation of metal vapors in cooler regions of the weld pool. These vaporization rates place upper limits on the surface temperature of the weld pool. These limits are in good agreement with measurements on different alloys when using electron beam welding, but the results for arc welding are somewhat lower than the temperatures often assumed for arc weld pools. It is concluded that the metal vaporization from the weld pool places a limit on the maximum temperature of the pool which is significantly less than the boiling temperature of the metal. The presence of volatile alloying elements may further reduce this maximum temperature limit.

Table IV indicates that apparent evaporation rates (initial and mean) confirm Zn domination of the group I alloys, Mg domination in group II, and co-domination of Zn and Mg in group III alloys.

The largest absolute evaporation seen occurs in the Zn dominated group I followed by Mg dominated group II. The apparent percentages of the total energy are very small indicating that the vapors are subjected to multiple recycling during extended time arc welding.

Table IV. Comparison of Predicted Welding Temperatures and Temperatures Measured by Schauer *et al.*¹¹

Al-Alloy, Steel or Metal	Maximum Predicted Temperatures (CSM) if 10 Pct or 100 Pct Energy Went into Evaporation	Dominating Vapor Species at CSM if		Schauer's ¹¹ Electron Beam Temperatures t $^\circ\text{C}$
		10 Pct Went into Evaporation	100 Pct Went into Evaporation	
Aluminum	1775 2091	Al	Al	
1100	1614 2091	Zn	Al	1900 ± 100 (1990 to 2055)*
2024	1290 1751	Mg	Mg	1700 ± 100
5083	1126 1491	Mg	Mg	1250 ± 100
5456	1104 1451	Mg	Mg	
6061	1358 1882	Mg	Mg	1800 ± 100 (1800 to 1890)*
7075	909 1242	Zn	Zn	1080 ± 100 (1380 to 1485)*
Steels with 0.5 pct Mn	2190 2520	Mn	Fe	2290 ± 60 ; HY-130 st
Steels with 2.0 pct Mn	2010 2520	Mn	Fe	2100 ± 50 ; 304 st
20-6-9 steel		Mn	Mn	1820 ± 40
Tantalum		Ta	Ta	4400 ± 150

*Data from Schauer's figures, not matching tabulated temperatures

ACKNOWLEDGMENTS

The authors wish to express their appreciation to the Office of Naval Research for sponsoring this research under contract N00014-C-80-0384, and to Dr. Charly Allemand for assistance with setting up the spectrographic equipment.

REFERENCES

1. D. W. Moon and E. A. Metzbower: *Welding Journal*, 1983, vol. 62, pp. 53s-58s.
2. S. S. Glickstein: *Welding Journal*, 1976, vol. 55, pp. 222s-29s.
3. R. F. Heile and D. C. Hill: *Welding Journal*, 1975, vol. 54, pp. 201s-10s.
4. J. D. Cobine and E. E. Burger: *J. Appl. Phys.*, 1955, vol. 26, pp. 895-900.
5. A. Block-Bolten and T. W. Eagar: *Trends in Welding Research in the United States*, S. A. David, ed., ASM, Metals Park, OH, 1982, pp. 53-73.
6. S. Dushman and J. M. Lafferty, eds., 2nd Edition, *Scientific Foundations of Vacuum Technique*, John Wiley, New York, NY, 1962, pp. 691-737 and pp. 15-21.
7. O. H. Nestor: *J. Appl. Phys.*, 1962, vol. 33, pp. 1638-48.
8. N. Christensen, V. Davies, and K. Gjermundsen: *British Welding J.*, 1965, vol. 12, pp. 54-75.
9. M. B. C. Quigley, P. H. Richards, D. T. Swift-Hook, and A. E. F. Gick: *J. Phys., D-Appl. Phys.*, 1973, vol. 6, pp. 2250-58.
10. G. Dunn: M.I.T., Cambridge, MA, unpublished research, 1982.
11. D. A. Shauer, W. H. Giedt, and S. M. Shintaku: *Welding Journal*, 1978, vol. 57, pp. 127s-33s.
12. R. Hultgren, P. D. Desai, D. T. Hawkins, M. Gleiser, and K. K. Kelley: *Selected Properties of Binary Alloys*, ASM, Metals Park, OH, 1973.

METAL VAPORS IN GAS TUNGSTEN WELDING ARCS

by

Gregory J. Dunn

Submitted to the Department of Materials Science and Engineering
on August 10, 1984 in partial fulfillment of the requirements for the degrees of
Bachelor of Science in Materials Science and Engineering
and
Master of Science in Materials Engineering

ABSTRACT

Metal vapors in gas tungsten welding arcs were studied in order to determine the effects of these vapors on arc properties and subsequently on weld bead configuration. Emission spectroscopy and monochromatic photography were used to determine the composition and distribution of vapors in arcs on stainless steel. It was found that, in addition to the expected species (Fe, Mn, Cr), calcium and aluminum vapors were also detectable, even at very low base-metal concentrations. All metal vapors were determined to be concentrated just above the weld pool in high current arcs, but also present in the upper regions of low current arcs. Aluminum and calcium were also found to vaporize from the tungsten electrode.

Theoretical calculations of the plasma transport properties revealed that small amounts of low ionization potential elements such as aluminum or calcium do not have as great an effect on the electrical and thermal conductivities as has been previously reported if the presence of other metal vapors such as iron or manganese is also considered.

It is therefore concluded that the effects of minor elements on arc properties may be less important than has previously been believed in explaining the variable penetration often associated with minor element additions to the base metal, and that weld pool convection effects such as surface tension modifications are probably more important. However, the effects of vapors emitted by the tungsten electrode may have a great effect on arc properties, as the shielding gas is otherwise free of contaminants in the upper regions of the arc.

Thesis supervisor: Thomas W. Eagar
Title: Associate Professor of Materials Engineering

Appendix C

(presented at AIME Annual Meeting, New York, NY, February 1985)

CHARACTERIZATION OF MOLTEN WELD POOL

by

J. Szekely, T. W. Eagar, J. McKelliget, and G. Dunn

ABSTRACT

A complete understanding of heat and fluid flow in the molten weld pool requires an understanding of processes occurring within the arc plasma itself. Through the simultaneous solution of Maxwell's equations, the Navier-Stokes equation and the heat balance equation in the plasma, one can predict the temperature, fluid flow and electric current fields in the plasma. This permits one to estimate the fraction of heat conducted to the workpiece by the current and by convection. It is further shown that these fields can be perturbed by the introduction of metal vapors within the plasma. Experimental studies confirm that these vapors are not homogeneously distributed throughout the plasma, hence, the complete solution to this problem becomes formidable although not intractable.

SPECTROMETRIC TEMPERATURE MEASUREMENTS
OF THERMAL RADIATORS

by

GORDON BRUCE HUNTER

Submitted to the Department of Materials Science and Engineering
on May 4, 1984 in partial fulfillment of the requirements
for the Degree of Doctor of Philosophy in Metallurgy

ABSTRACT

It is demonstrated that the temperature of a thermal radiator can be determined by multiple spectral radiance measurements without prior knowledge of the emissivity of the source. This new passive measurement technique assumes only that a smooth function exists between spectral emissivity and wavelength. The spectral radiance values are fit to a Planck radiation law relation to yield the temperature of the source. Computer simulations are included to show that relative errors in the temperature measurements are generally an order of magnitude less than relative errors in the spectral radiance measurements and in the simultaneously calculated spectral emissivity values.

A Multichannel Infrared-Red Temperature Micro-Analyzer (MIRTMA) system is described. This early prototype instrument is capable of monitoring temperatures above 1100 K with a spatial resolution of 100 μm and a temporal resolution of 3 s using spectral radiance measurements at approximately 200 wavelengths in a range of 0.6-0.8 μm . Demonstrations of this equipment on a heated platinum strip source are described and discussed. The temperature measurements of these sources are generally within 5% of the actual temperature, but can be within 1% using certain techniques.

Capabilities and limitations of the method and the MIRTMA equipment are presented. The various calibrations used with the technique are also explained, particularly with respect to corrections for the nonlinear response of the Silicon Intensified Target detector employed as part of the MIRTMA. Potential improvements to the method and instrument based on this work are presented.

Thesis Supervisor : Dr. Thomas W. Eagar

Title : Associate Professor of Materials Engineering

An improved method of multi-wavelength pyrometry

Gordon B. Hunter, Charly D. Allemand, and Thomas W. Eagar

Materials Processing Center, Massachusetts Institute of Technology
Cambridge, Massachusetts 02139Abstract

It is demonstrated that the temperature of a thermal radiator can be determined by curve fitting techniques using multiple spectral radiance measurements without prior knowledge of the emissivity of the source. This new passive measurement technique assumes only that a smooth function exists between spectral emissivity and wavelength. The spectral radiance values are fitted to a Planck radiation law relation to yield the temperature of the source. Error analysis shows that relative errors in the temperature measurements are generally an order of magnitude less than in the spectral radiance measurements and in the simultaneously calculated spectral emissivity values. Computer simulations are included which show the effects of varying different parameters, such as the number of data pairs, the wavelength range, the spectral emissivity behavior, the source temperature, and the measurement noise, on the accuracy of the temperature determination. Experimental confirmation of this technique is presented showing temperature measurements within 1% of the actual temperatures on a platinum surface within a temperature range of 1273-1724 K.

Introduction

One of the greater problems faced by spectrometric methods of temperature measurement is characterization of the emissivity of the source. The most widely used types of radiation pyrometry are based on an approximation of the Planck radiation law and an assumption of constant spectral emissivity in the observed wavelength band. Ratio pyrometry techniques, such as the two color method, are examples of this¹⁻³. Other methods require that emissivity be determined separately from the temperature to obtain accurate thermal measurements.

One class of techniques, referred to as multi-wavelength pyrometry, has been developed to calculate both the temperature and emissivity of a thermal radiator employing one set of radiation measurements from several wavelengths⁴⁻⁶. Typically, these techniques involve assuming a functional dependence between spectral emissivity and wavelength, and then using the radiation measurement data to determine the adjustable emissivity parameters and temperature by solving simultaneous equations. The main disadvantage with these methods is the sensitivity of the accuracy to radiation measurement errors⁶.

An improvement to this approach is to use a much larger number of radiation measurements to determine the temperature and emissivity parameters using curve fitting techniques. The sensitivity to measurement errors is greatly reduced by the statistics involved with curve fitting a large number of measurements. The only assumption necessary for this technique is that a smooth function exists between spectral emissivity and wavelength over the wavelength range of the radiation data.

Theory

Provided that the source is a thermal radiator, the spectral radiance (N_λ in units of $\text{W/cm}^2\text{-}\mu\text{m}\text{-sr}$) emitted is function of the wavelength (λ in μm) of the radiation, the temperature (T in K) of the source, and the spectral emissivity (ϵ_λ) of the emitting surface according to the Planck radiation law:

$$N_\lambda = \epsilon_\lambda C_1 / (\lambda^5 (e^{C_2/\lambda T} - 1)) \quad (1)$$

where C_1 ($11910 \text{ W}\cdot\mu\text{m}^2/\text{cm}^2\cdot\text{sr}$) and C_2 ($14387.9 \mu\text{m}\cdot\text{K}$) are the Planck radiation constants^{1-2,7}. Typical Planck radiation law curves are shown in Figure 1. Emissivity is a function of many variables⁸, however all but wavelength are constant if the spectral radiance measurements are simultaneous and optically identical.

Because it has been difficult to establish an analytical expression, spectral emissivity has been represented in many studies by a simple series of terms with adjustable parameters, a polynomial for instance, valid in a restricted wavelength range^{3,6}. Substituting the assumed spectral emissivity function into Equation 1 yields the spectral radiance relation as a function of only wavelength at a constant temperature. The temperature and coefficients of the emissivity relation are obtained simultaneously by curve fitting the spectral radiance measurements for a large number of wavelengths to the spectral radiance function. This eliminates the need to determine emissivity separately from the temperature.

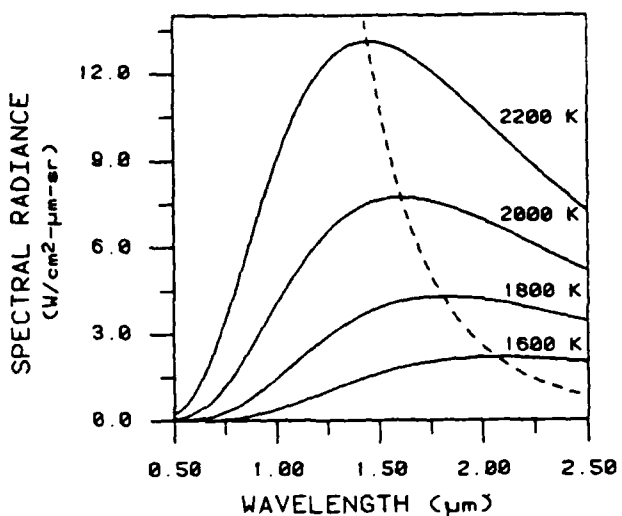


Figure 1. Planck radiation law curves with a constant spectral emissivity ($\epsilon_\lambda = 1$) for four temperatures. The dotted line denotes the locus of curve maxima for all temperatures and this spectral emissivity.

The insensitivity of the temperature determination to errors in the spectral radiance measurements can be shown analytically by differentiating Equation 1 and substituting the relations:

$$Z = C_2 / \lambda T \quad (2)$$

$$Y = Z / (1 - e^{-Z}) \quad (3)$$

into the result to obtain:

$$dN_\lambda / N_\lambda = d\epsilon_\lambda / \epsilon_\lambda + Y dT / T \quad (4)$$

For the range of wavelengths and temperatures examined in this study, Y is about one order of magnitude. Thus, a relative error in the spectral radiance data will cause at most an equal relative error in spectral emissivity or about an order of magnitude less relative error in temperature. The precision in the emissivity and temperature determinations are further increased due to the statistical nature of the curve fitting analysis.

As can be deduced from Equation 4, correlation effects between the adjustable parameters, even in the absence of experimental error in the spectral radiance ($dN_\lambda / N_\lambda = 0$), can cause errors in the temperature determination:

$$d\epsilon_\lambda / \epsilon_\lambda = -Y dT / T \quad (5)$$

Application

The eventual goal of this work is to produce an instrument and technique to measure surface temperatures of molten gas-tungsten arc weld pools. Most previous studies of weld pool temperatures have employed thermocouples⁹⁻¹⁰. These techniques have been far from optimal since the thermocouples impede fluid motion in the pool and may alter the thermal profile¹. To avoid contact with the weld pool some investigators have used total radiation pyrometry to map isotherms on and around the weld pool¹¹⁻¹³, however the difficulty in determining the emissivity has prevented them from accurately associating these isotherms with absolute temperatures.

Recent advances in multichannel photoelectric detectors allow the simultaneous spectral radiance measurements at multiple wavelengths. Coupled with the rapid data processing capabilities of computers, these detectors make practical the improved pyrometric technique described above. This technique has the potential for eliminating the problems encountered with thermocouples or emissivity in other studies, as well as making accurate thermal measurements.

An instrument was built to experimentally demonstrate the technique and serve as a prototype for eventually measuring weld pool surface temperatures¹⁴. The instrument is named the

Multichannel Infrared-Red Temperature Micro-Analyzer (MIRTMA). The MIRTMA is divided functionally into three parts: the infrared microscope, the detector system, and the data processor. The infrared microscope is comprised of the spectrograph, which disperses the radiation onto the photodetector surface, and of the focusing optics, which image a 100 μm effective source area onto the spectrograph. The detector system measures the photon irradiance and provides experiment synchronization capabilities, while the data processor is used to calibrate the detector response to spectral radiance and analyze the calibrated data to determine the source temperature. The detector selected for this study is a Silicon Intensified Target (SIT) vidicon detector purchased from EG&G Princeton Applied Research Corporation¹⁴⁻¹⁵. The spectral radiance from approximately 200 channels (of the available 500) of wavelength in the range 0.60-0.80 μm were measured since only these channels registered significant signals.

Once the spectral radiance data has been obtained, the data processor uses a curve fitting routine to calculate the temperature. For the purposes of curve fitting, the spectral emissivity is assumed to follow each of three relations in turn:

$$\epsilon_\lambda = \epsilon_{01} + \epsilon_{11} \lambda \quad (6)$$

$$\epsilon_\lambda = \epsilon_{02} + \epsilon_{12} \lambda + \epsilon_{22} \lambda^2 \quad (7)$$

$$\epsilon_\lambda = e^{(\epsilon_{03} + \epsilon_{13} \lambda)} \quad (8)$$

where ϵ_{ij} are constant coefficients for the particular experimental conditions. Equation 8 is employed by Svet for his multi-wavelength technique³.

The curve fitting routine is a two step process. Initially, a value for the temperature is assumed to determine the emissivity coefficients of the linear spectral emissivity function (Equation 6) by a least squares method¹⁶. By repeating this process, the routine searches for a temperature which will yield a minimum ϵ_{11} term. The temperature that is found is then used to calculate a mean emissivity value:

$$\epsilon_\lambda = \epsilon_{00} \quad (9)$$

This provides approximations of temperature and emissivity which are used as the starting point for the second step of the process.

Next, the routine uses a least squares fit with a gradient expansion search algorithm¹⁷ to find the emissivity coefficients and the temperature using each spectral emissivity function above in turn. The method involves expanding the fitting function in a Taylor's expansion with the adjustable parameters of the spectral emissivity function and temperature, then uses a least squares method to find the optimum values of these parameters. These optimum values are chosen by minimizing the reduced chi-squared value for the fit so that the relative decrease in the chi-squared value for small changes in the parameters is reduced below a threshold (0.01%).

Computer simulations

To demonstrate the improved multi-wavelength technique, a series of computer simulations were devised. Theoretical spectral radiance data was generated using the Planck radiation law (Equation 1) for a given schedule of temperature, emissivity function, wavelength range, and number of data pairs (see Table 1). A temperature of 1800 K was chosen for most schedules since this is the approximate melting temperature of steel. To simulate experimental noise, the generated Planck law values were multiplied by a random number series of uniform distribution around unity. This is not necessarily the form of noise expected in practice, but for simplicity the noise was assumed proportional to the spectral radiance. The rms value of the difference between the random number series and unity is used to describe the three simulated experimental noise levels: 0.008, 2.85%, and 5.70%.

Table 1. Schedules of Parameters for the Computer Simulations

Schedule	T (K)	ϵ_λ	Data Pairs	λ Range (μm)
1	1800	1.0	200	0.6 - 0.8
2	1273	1.0	200	0.6 - 0.8
3	1800	1.6 - 1.0 λ	200	0.6 - 0.8
4	1800	1.0	100	0.6 - 0.8
5	1800	1.0	200	0.5 - 1.5

These generated data sets were used to simulate measured data for the curve fitting routines. For each noise level, a mean and standard deviation for the adjustable parameters were calculated by repeating the procedure with 20 different sets of data for each schedule. The mean and standard deviation of the temperature parameter, which give an indication of

the errors and scatter in the temperature measurements, are shown relative to the actual temperature in Figures 2-5. The results for two noise levels of Schedule 3 are given in Table 2.

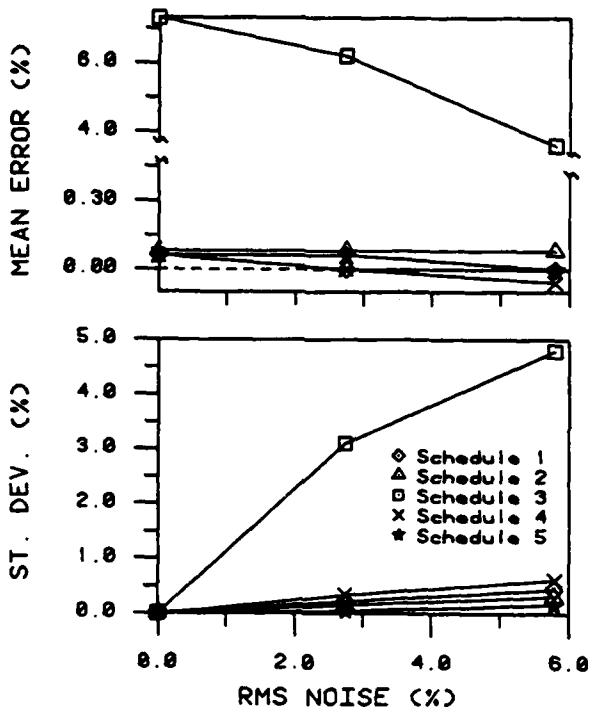


Figure 2. Computer simulation results for the constant emissivity assumption (Equation 9). The mean temperature measurement error relative to the actual temperature is above (note the change of scale) with the relative standard deviation of the measurements below.

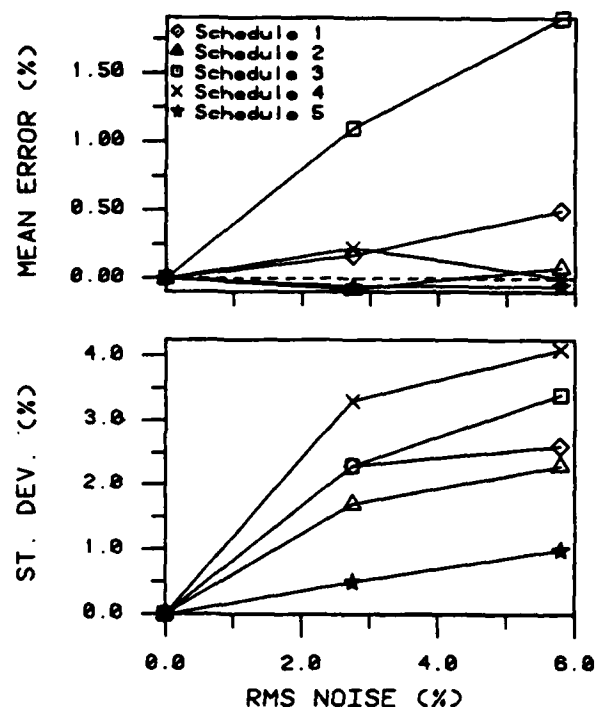


Figure 3. Computer simulation results for the two term polynomial emissivity assumption (Equation 6). The mean temperature measurement error relative to the actual temperature is above with the relative standard deviation of the measurements below.

Table 2. Mean Parameter Results of the Schedule 3 ($\varepsilon_1 = 1.6 - 1.0\lambda$) Simulation (Standard Deviations in Parentheses)

Rms Noise (%)	ε_λ Fitting Equation	T (K)	ε_0	ε_1	ε_2
0.00	9	1931	0.41	-1.00	-0.48
	6	1800	1.60		
	7	1831	0.94		
	8	1752	1.30		
5.70	9	1864 (86)	0.72 (0.40)	-0.83 (0.93)	-0.47 (0.62)
	6	1834 (61)	1.37 (0.98)		
	7	1855 (53)	0.82 (0.39)		
	8	1784 (98)	0.94 (1.33)		

As can be seen, the introduction of as much as 5.7% rms noise causes less than a 0.5% relative mean temperature error, with less than a 5% relative standard deviation, for most schedules and spectral emissivity assumptions. Table 2 shows that the errors and scatter tend to be much larger for the emissivity parameters than for the temperature determination, which is typical of all of the simulations. This behavior is as expected from the analysis of Equations 4 and 5. Also consistent with this analysis is the reduction in most errors and scatter for the lower temperature simulation (Schedule 2) due to the increase in λ value (Equation 3) compared to the higher temperature (Schedule 1). Reducing the number of data pairs from 200 (Schedule 1) to 100 (Schedule 4) generally caused an increase in the mean error and standard deviation, as is expected by curve fitting statistics.

In the wavelength regions and temperatures examined, the Planck radiation law appears roughly exponential in nature, as can be seen in Figure 1. Thus, especially with the exponential fitting function (Equation 8), there is a possible ambiguity between the effects of a change in the temperature or emissivity parameters that cannot be resolved by the curve fitting routines and results in a correlation between these parameters. As is expected from this, the mean errors and standard deviations are usually greatest for the exponential emis-

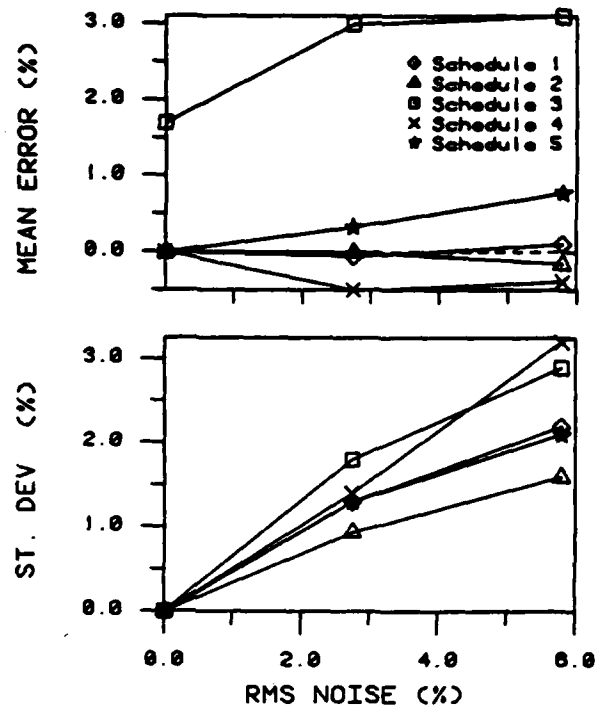


Figure 4. Computer simulation results for the three term polynomial emissivity assumption (Equation 7). The mean temperature measurement error relative to the actual temperature is above with the relative standard deviation of the measurements below.

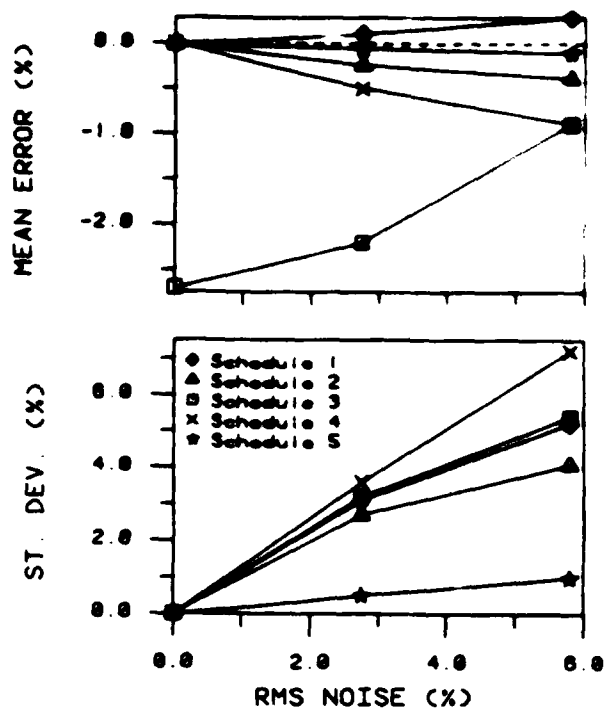


Figure 5. Computer simulation results for the two term exponential emissivity assumption (Equation 8). The mean temperature measurement error relative to the actual temperature is above with the relative standard deviation of the measurements below.

sivity function. Extending the wavelength range to 0.5-1.5 μm (Schedule 5) greatly reduces these values, especially for the exponential function, since the Planck radiation law curve does not approximate a linear exponential function in the extended range.

The generated spectral emissivity values for Schedule 3 drop linearly from 1.0 to 0.8 as the wavelength increases from 0.6 to 0.8 μm . The constant and exponential emissivity fitting functions are expected to have difficulty fitting this behavior and thus cause errors in the temperature measurement. However, the two and three term polynomial emissivity fitting functions would be expected to make more accurate temperature measurements. In fact aside from the two term polynomial emissivity with no noise, the largest mean temperature measurement errors occur with Schedule 3. Correlation effects between the fitting parameters are again the cause. A clear example of this is seen in Table 2 comparing the measured polynomial emissivity parameters for data with no noise. In the absence of correlation between the parameters, the results for the two and three term polynomial functions should be identical (with $\epsilon_{22} = 0$ from Equation 6).

The effect of a temperature gradient within the source area was also simulated. For simplicity, the source is assumed to be divided in equal parts symmetrically to an average temperature so that half of the source is at a lower temperature and half of the source is at a higher temperature. This is a condition which is more severe than would actually exist. Three gradients are compared using the parameters of Schedule 1 of Table 1: 0.0% (1800 K), 1.0% (1791 and 1809 K), and 10% (1710 and 1890 K). The results of these simulations are shown in Table 3. Even with this extreme approximation for the gradient, the measurement errors relative to the average temperature (2.4-3.8% for the 10% gradient) are less than the gradient itself. In addition, it can be seen that even with thermal gradients on the order of 1% in the measured area, the fitting routine will find the correct average temperature.

Experimental demonstration

To demonstrate the technique experimentally, the temperature of a resistively heated platinum strip was measured using the MIRTMA system. The spectral emissivity behavior of this source was unknown. The temperature of the source area on the strip was monitored with a thermocouple for comparison with the MIRTMA results. Measurements were made at four tem-

peratures within 1270-1725 K and the results are shown in Figure 6. More detailed descriptions of these measurements and the MIRTMA are being prepared for publication and are also included in Reference 14.

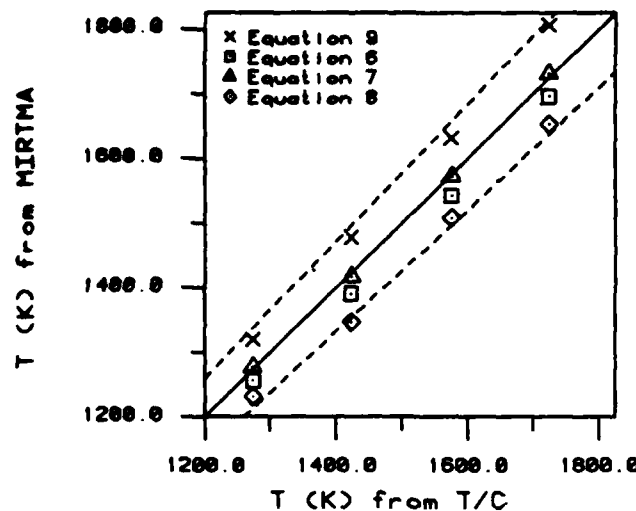


Figure 6. Comparison of the MIRTMA measurements to the thermocouple (T/C) measurements of the platinum strip source (perfect agreement and 5% error bands are denoted by solid and dotted lines respectively).

The MIRTMA temperature measurements are generally within 5% of the thermocouple measurements, and are within 0.5% for the three term polynomial emissivity fitting function. The inability of the constant function to adequately fit the actual spectral emissivity behavior accounts for the errors with that function, and correlation effects are the cause of the large errors with the exponential function.

Summary

This paper describes an improved method of multi-wavelength pyrometry which uses curve fitting techniques. This method fits multiple spectral radiance measurements to the Planck radiation law relation to determine temperature and spectral emissivity simultaneously. It assumes only that a smooth function exists between spectral emissivity and wavelength over the range of the observed wavelength band. Relative errors in the temperature measurements are generally an order of magnitude less than random relative measurement errors of spectral radiance and than relative errors in the calculated spectral emissivity values.

Computer simulations show that the accuracy and precision of the technique increases as the wavelength range is extended toward the peak in spectral radiance and as the number of measured data pairs increases. Simulations also show that thermal gradients of approximately 1% of the average temperature within the source area cause negligible errors in the temperature measurement. The MIRTMA system has experimentally confirmed that this technique can be used to measure temperatures of a platinum strip within 1274-1724 K. These thermal measurements agreed with thermocouple measurements to within 5% for all assumed forms of the emissivity fitting function and within 0.5% for the three term polynomial emissivity function.

Errors may be caused in the temperature measurements if the assumed functional form of spectral emissivity with wavelength has too few terms to fit, or is otherwise inappropriate for the actual behavior. This problem is exacerbated by correlation effects between the temperature and emissivity parameters during curve fitting with the current procedures. Further work is being conducted to improve the fitting procedure and minimize correlation effects between the adjustable parameters. Reducing correlation effects should increase the temperature measurement accuracy and shorten the computation time. Studies are also being conducted to determine the proper emissivity function and its limits of validity.

Acknowledgements

Support for this research is provided by the Office of Naval Research under Contract N00014-80-C-0384. The authors are also grateful to Mr. Carl Sorensen of MIT for many

Table 3. Temperature Results (in K) of the Thermal Gradient Simulations

Gradient of T (%)	ε) Fitting Equation			
	9	6	7	8
0.0	1801	1800	1800	1800
1.0	1801	1801	1801	1801
10.0	1844	1865	1868	1863

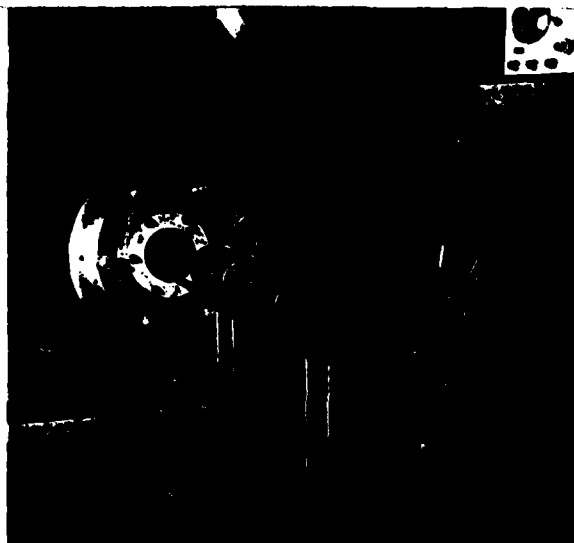
useful discussions.

References

1. E. O. Doebelin, Measurement Systems - Applications and Design, Chap. 8, McGraw-Hill, New York (1983).
2. H. D. Baker, E. A. Ryder, N. H. Baker, Temperature Measurement in Engineering, Vol. 2, Chap. 3, Omega Engineering, Stamford (1975).
3. D. Ya. Svet, High Temperatures - High Pressures 4(6), 715 (1972).
4. D. Ya. Svet, Sov. Phys. Dokl. 20(3), 214 (1975).
5. D. Ya. Svet, Sov. Phys. Dokl. 21(3), 162 (1976).
6. P. B. Gates, Metrologia 17(3), 103 (1981).
7. R. D. Hudson, Jr., Infrared Engineering, Chap. 2, John Wiley, New York (1969).
8. R. Siegel and J. R. Howell, Thermal Radiation Heat Transfer, Chap. 5.3, McGraw-Hill, New York (1972).
9. R. L. Apps and D. R. Milner, Brit. Weld. J. 10(7), 348 (1963).
10. V. P. Chernysh, V. D. Kuznetsov, and E. V. Turyk, Autom. Weld. 29(7), 3 (1976).
11. N. D. Malmuth, W. F. Hall, B. J. Davies, and C. D. Rosen, Weld. J. 53(9), 388 (1974).
12. W. E. Lukens and R. A. Morris, Weld. J. 61(1), 27 (1982).
13. B. A. Chin, N. H. Madsen, and J. S. Goodling, Weld. J. 62(10), 227s (1983).
14. G. B. Hunter, Ph.D. thesis, MIT, Cambridge (1984).
15. R. K. Chang and M. B. Long, in Light Scattering in Solids II, M. Cardona and C. Guntherodt, eds., p. 179, Springer-Verlag, New York (1982).
16. P. R. Bevington, Data Reduction and Error Analysis for the Physical Sciences, p. 134, McGraw-Hill, New York (1969).
17. P. R. Bevington, Data Reduction and Error Analysis for the Physical Sciences, p. 232, McGraw-Hill, New York (1969).

A Method of Filming Metal Transfer in Welding Arcs

Standard optical components and a small He-Ne laser are used to observe metal transfer in welding arcs



Photographic apparatus for high speed filming of metal transfer in CMAW and SMAW arcs. Red light is the collimated laser beam used to illuminate the arc area

BY C. D. ALLEMAND, R. SCHOEDER, D. E. RIES, AND T. W. EAGAR

During studies of metal transfer in gas metal arc or shielded metal arc welding, it is often useful to perform high speed cinematography of the transfer process; however, the high light emission from the arc creates a number of practical problems. The conventional solution is to flood the arc area with a light source of even greater intensity than the arc. This very intense light is then photographed through a very strong neutral density filter. While this approach provides a very good image of the metal transfer, the external light source is relatively expensive, and the severe filtering of the arc light can result in loss of structural information about the arc plasma.

This article describes an optical layout that has been used to take moving pictures of a filler metal wire and droplets in a gas metal arc. More generally, the apparatus is applicable to observation of an opaque object surrounded by a bright and transparent light source of such high intensity that it blinds the detector and prohibits direct observation.

This article describes an apparatus that produces a shadowgraph of the electrode and the detaching metal drops. The system can also be used with interchangeable filters that permit a portion of the arc light to be transmitted, thus providing additional information about the arc plasma.

The Shadowgraph

The 0.8 mm (0.030 in.) diameter output beam of a 2 mW He-Ne laser is expanded and spatially filtered into a 20 mm (0.79 in.) diameter collimated beam and used to illuminate the object represented in Fig. 1 by an opaque sphere. Since the plasma surrounding the object is transparent at 633 nm, the collimated laser light passes through the plasma and is concentrated by lens 1 (placed at a distance of twice its focal length from the sphere) into the hole of a diaphragm placed at the focus of the lens. A narrow band interference filter which transmits at the laser wavelength is placed behind the diaphragm. All the laser light passes through this filter, except the part blocked by the opaque sphere and a small fraction which is absorbed by the filter. This simple apparatus may

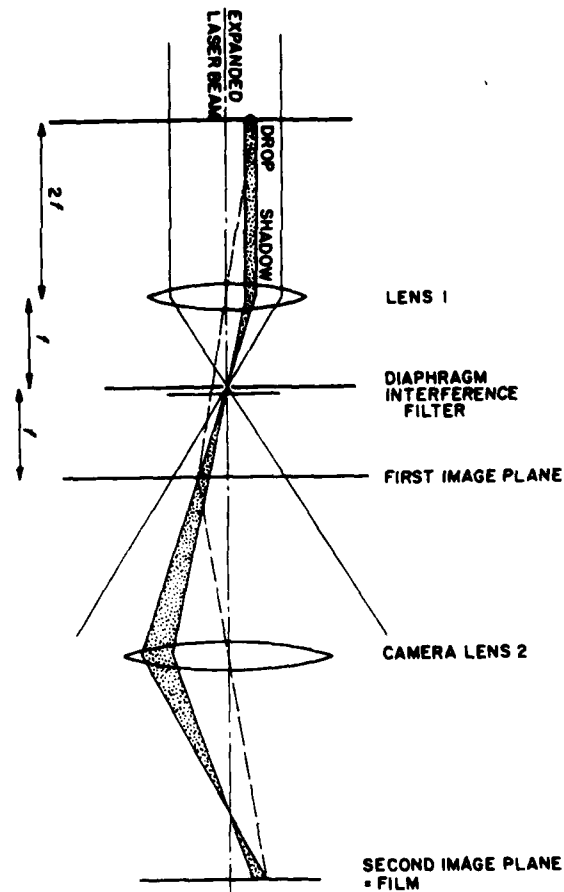


Fig. 1—Simplified optical diagram of the shadowgraph, showing the way spatial and interference filters were used to block off arc light and admit laser light only. Note that in this diagram the laser beam overfills the camera lens. An opaque drop is shown in the object area and its shadow is traced to the film. The image position and height are indicated by the intersection of the image plane and field ray. The chief ray through the center of each imaging lens is represented by a dashed line

C. D. ALLEMAND, R. SCHOEDER, D. E. RIES, and T. W. EAGAR are with the Department of Materials Science and Engineering, Massachusetts Institute of Technology, Cambridge, Mass.

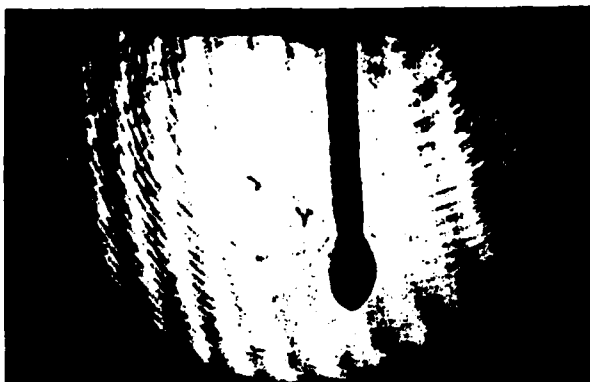


Fig. 2 - 16 mm movie shadowgraph obtained with the shadowgraph of Figure 1, to which a field lens has been added. The filler metal wire and a falling droplet are clearly visible, but the arc is not recorded. The interference rings are due partly to the absence of a spatial filter in the beam expander and partly to the presence of a narrow band interference filter

thus be used to form a shadowgraph of the sphere. The image is produced at one focal length of lens q behind the diaphragm and is relayed to the high speed camera film plane by lens 2 of the camera.

To understand how the light from the arc is excluded from the shadowgraph, one must remember that light from the arc is not collimated but is emitted in all directions. The arc light is not focused on the diaphragm, and most of it is rejected at this point. The small portion of arc light that passes through the diaphragm (which acts as a spatial filter) is rejected by the narrow band interference filter. The arc light is nearly completely blocked by both the spatial and the wavelength filter, and only the laser light reaches the film to produce a red background with a sharp shadow of the object, as seen in Fig. 2.

The resolution of the image is limited by the diaphragm and by the quality of the imaging optics. Use of good quality 35 mm camera lenses and reasonably large diaphragm openings (e.g., 1.5 to 3 mm) have produced acceptable resolution.

There are a number of considerations which make this system more practical:

1) The object on the first image plane is reversed such that the camera records an upside-down picture. This is reversed by adding another lens (lens 2, Fig. 3) that produces a secondary, upright image. This lens can also be used as a relay lens to increase the distance from the object to the camera.

2) The camera lens diameter (lens 4, Fig. 3) is usually much smaller than the beam diameter at the level of the camera lens. Therefore, much of the field is lost; however, this may be restored to full object size by a field lens (lens 3) placed on the second image plane.

3) The camera lens has a diaphragm that is normally used to adjust the film exposure. In the directed light system described, light from a point in the object area reaches a well-defined and small part of the camera lens. Therefore, the camera lens diaphragm does not act as a normal aperture stop, but rather as a field stop. Since this is not desirable, the camera lens diaphragm is kept wide open and the exposure is adjusted by means of neutral density filters. The exposure was measured roughly by means of a 35 mm still camera before test runs with the high speed camera were made. The aperture of the 35 mm camera was opened wider than the beam, and the focal length of its lens was taken into account to estimate the correct exposure for the high speed movie.

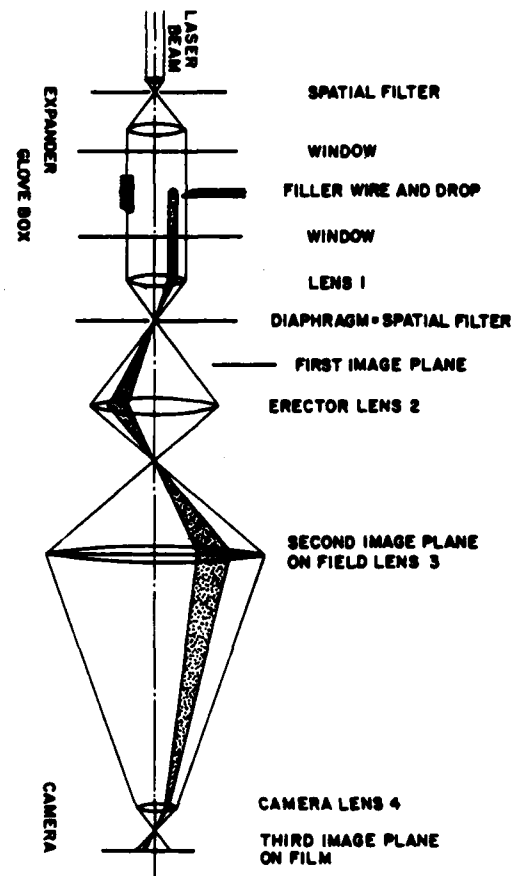


Fig. 3 - Complete optical layout. The interference filter has been removed to allow enough arc light through the optical train for the film to record the arc path. An erector lens and a field lens have been added. See text for details

4) When studies are performed in a glove box, the laser beam can be introduced into and led out of the glove box through glass windows, also shown in Fig. 3. These windows should be polished plane parallel glass tilted about 5 degrees

Table 1—Equipment Specifications

Laser:	Spectra Physics, 2 mW He-Ne Model 145-02
Expander with spatial filter:	Spindler & Hoyer 258 Model 038655
Lens 1:	f 150 mm, 6 elements, self-designed ^(a)
Neutral density filter:	ND 0.5, OPCO Labs, Leominster, Mass.
Erector lens:	Mamiya/Sekor 1:2/50
Diaphragm:	NRC Model 1D-1.5 opened 1.5 mm
Interference filters:	633 nm, Andover Corp., Lawrence, Mass.
Field lens:	f 200 mm bi-concave simple lens, 40 mm diameter
Camera lens:	Schneider Tele-Xenar 1:2.8/75
Spacer ring:	10 mm
Camera:	Redlake Hycam, model 41
Optical benches and accessories:	Klinger Scientific

^(a)This lens may be replaced by a commercial f 150 mm photographic or reproduction lens with a clear aperture of 25 mm or more.

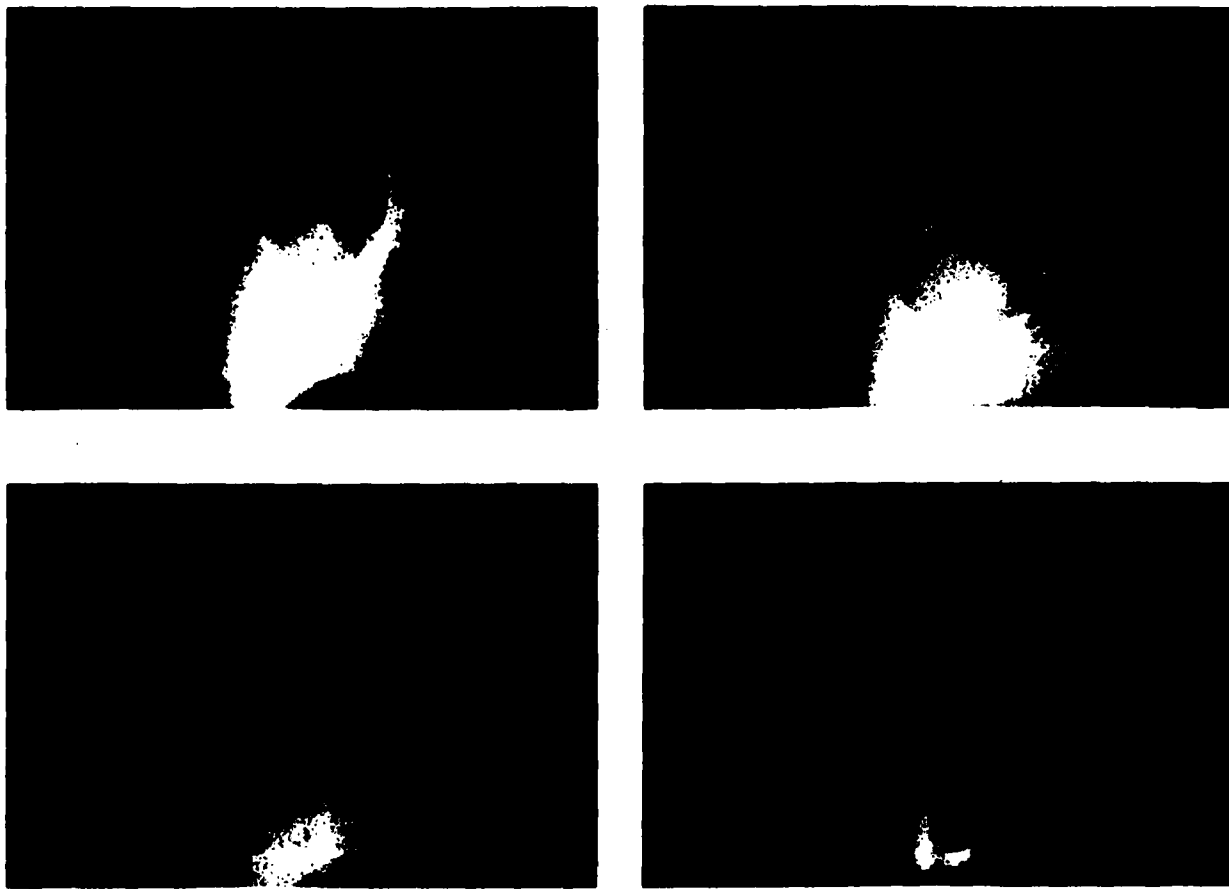


Fig. 4—Gas metal arc welding of titanium: Top Left—Cathode plasma jet forms; Top Right—jet repels metal drop; Bottom Left—drop detaches, jet breaks; Bottom Right—jet broken. Replacement of the narrow band filter with the neutral density filter provides more information on the behavior of the plasma as well as the droplet detachment

from vertical to prevent a second surface reflection from following the main optical path.

Addition of Arc Light Illumination

The shadowgraph apparatus produces a black image on a red background, without information on the droplet surface or even on the arc itself. Some of this information can be retrieved if one removes the 633 nm laser filter, thus letting some of the arc light through the system. The balance between the laser and the arc light is reached by adjusting the diameter of the diaphragm hole and by adding a neutral density filter where the narrow band filter had been located.

This produces an image of the electrode and droplets which is back-illuminated by the red laser light and front-illuminated by the blue arc light—Fig. 4. The arc itself is clearly visible and can be allowed to overexpose as a white image on the film. The instrument specifications of this system are given in Table 1.

Conclusion

A method has been described which permits viewing of metal transfer in welding arcs using relatively inexpensive optical components and a small size He-Ne laser. In many cases, the optical information transferred by this method is superior to that obtained through use of intense external light sources and very dense neutral filters.

WEAR OF CONTACT TIPS IN GAS-METAL ARC WELDING OF TITANIUM

by

Jerome Lee LaPointe

Submitted to the Department of Mechanical Engineering
on June 4, 1984 in partial fulfillment of the
requirements for the degree of

Bachelor of Science

ABSTRACT

Wear in copper contact tips occurs much more rapidly in gas-metal arc (GMA) welding when titanium wire is used than when steel wire is used. This rapid wear necessitates frequent changing of contact tips, which is expensive. Experiments were run to understand the wear mechanisms and factors controlling wear in the contact tip. The results of the experiments reveal that titanium's low thermal conductivity causes melting of the wire at the contact tip-wire interface. Melted titanium can build up at the contact point and can lead to jamming of the wire in the contact tip or it can "freeze" to the moving wire and abrade the softer contact tip surface. Jamming of the wire in the contact tip did not occur in this experiment.

Thesis

Supervisor: Thomas W. Eagar

Title: Associate Professor of Materials Engineering

Appendix H

(presented at AIME Annual Meeting, New York, NY, February 1985)

CONTACT TIP WEAR IN GAS-METAL ARC WELDING OF TITANIUM

by

K. T. Ulrich, J. L. LaPointe, G. B. Hunter, and T. W. Eagar

ABSTRACT

When titanium wire is used in gas-metal arc (GMA) welding, copper contact tips wear more rapidly than when steel wire is used. This wear is accompanied by arcing between the base plate and the contact tip instead of between the plate and the filler wire, a phenomenon called "burnback." Burnback requires a complete shutdown of the welding operation and is therefore an expensive problem. Experiments were run to understand the mechanism of contact tip failure. The results of these experiments reveal that the low thermal conductivity of titanium causes melting to occur at the sliding electrical contact junction between the filler wire and the contact tip. Melting and subsequent freezing of titanium at the contact point can either build up and cause jamming of the filler wire in the contact tip or can cause adhesion of a chunk of titanium to the filler wire that then abrades the copper contact surface. The mechanism leading to the jamming of wire in the contact tip led to burnback in several of the experimental cases.

Influence of Arc Pressure on Weld Pool Geometry

A new model of a compound vortex is proposed as a possible mechanism to explain the deep surface depression encountered at currents over 300 amperes

BY M. L. LIN AND T. W. EACAR

ABSTRACT. At currents over 300 amperes, the surface of the weld pool becomes markedly depressed and the assumption of a flat surface is no longer valid. In order to predict the weld pool geometry, the shape of the surface depression under the action of the arc pressure has been calculated.

At currents of 300 amperes, it is found that the arc pressure cannot account for either the depth or the shape of the experimentally observed surface depression. Instead, a new model of a compound vortex is proposed as a possible mechanism to explain the deep surface depression in this current range.

Introduction

A number of investigators have studied the magnitude of arc pressure in gas tungsten arcs (Refs. 1-6). Some attempts have been made to explain the formation of several weld defects such as humped beads, finger penetration and undercutting (Refs. 6,7,8) based on the assumption that the arc pressure depresses the surface of the weld pool. An analytical model was developed by Friedman (Ref. 9) to simulate the distortion of fully penetrated molten pools in thin plates under the action of arc pressure and gravitational forces.

In our own experiments, we have studied the influence of welding currents on the depth and shape of the surface depression (Ref. 10). Surprisingly, it was found that the surface depression depth is very small (less than 1 mm, i.e., 0.04 in.)

at currents up to 240 amperes (A), but the depth increases rapidly as the current is increased by 30 A—Fig. 1. This rapid change in surface depression depth is difficult to explain by the increase in arc pressure which scales parabolically with weld current (Ref. 11). Arc pressure also will not explain why one current value (e.g., 260 A) can give either a depth of 1 mm (0.04 in.) or a depth of 5 mm (0.20 in.).

In order to evaluate whether arc forces of the magnitudes measured previously (Ref. 2) are capable of explaining the experimentally observed surface depression depths, an analytical model was developed. This model accounts for the balance of hydrostatic potential energy and surface energy with the work performed by the arc pressure displacing the liquid.

It will be seen that this model may be used to explain the experimental observations at low currents where surface depression is shallow; however, the

results cannot explain the experimental evidence obtained at high currents where the depth is significant. As a result, the assumption that arc pressure significantly alters weld pool geometry is no longer considered to be valid. Instead, a simplified convection model is proposed which can, in principle, explain the very deep surface depression of the weld pool at high currents.

Analytical Model

The surface depression will form a shape which minimizes the total energy; hence, calculus of variations may be used to calculate this shape under the action of arc pressure subject to the constraint that the volume of the weld pool is constant. In this model, it is assumed that there is no convection in the molten pool and that the weld is of the partial joint penetration type. In addition, for ease of analysis, cylindrical symmetry is assumed.

The energy to be minimized is the surface energy plus the potential energy of the liquid pool. Analytically, this takes the form

$$J = \int_{0}^{R} \sigma \cdot 2\pi r \left[1 + \left(\frac{dw}{dr} \right)^2 \right]^{\frac{1}{2}} dr + \int_{0}^{R} \rho g \cdot 2\pi (h - w) (H - \frac{h + w}{2}) dr \quad (1)$$

where the first integral on the right hand side of equation (1) is the interfacial energy between the gas and the liquid phase and the second integral is the potential energy of the liquid pool, with respect to a reference plane at $h = H$. The geometry of this system is shown in Fig. 2.

Equation (1) is subject to two constraints. First, constant liquid volume, which can be expressed as:

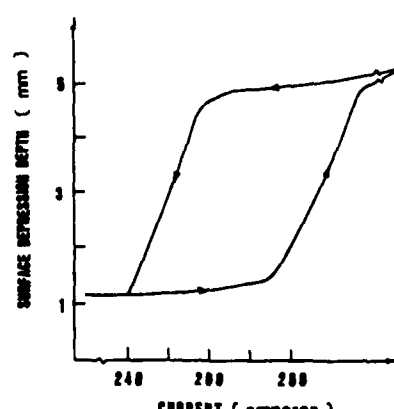


Fig. 1—Variation of surface depression depth with current, as observed experimentally. The arrows denote increasing and decreasing current and the fact that a hysteresis in surface depression exists as current is changed

Based on a paper presented at the 65th Annual AWS Convention held in Dallas, Texas, during April 8-13, 1984.

M. L. LIN and T. W. EACAR are associated with the Materials Processing Center, Massachusetts Institute of Technology, Cambridge, Massachusetts

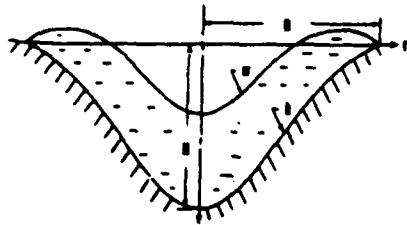


Fig. 2 - Geometry of depressed weld pool showing the definitions of several parameters used in this model

$$\int_0^R G_1 dr = \int_0^R \sigma 2\pi r w dr = 0 \quad (2)$$

where $G_1 = \sigma 2\pi r w$.

The second constraint requires that the work performed by the arc force be equal to the change of surface energy and potential energy of the liquid pool. However, the description of this constraint requires some discussion.

The first law of thermodynamics tells us that the energy of the system is conserved; however, the work performed by the arc force is not a state function but is path dependent. Consider the application of the arc pressure instantaneously. The volume of the liquid will be displaced by an amount ΔV and the work is $P\Delta V$; however, this work is not reversible.

The path of this form of work is given by ABC in Fig. 3 and the work is the area ABCD. If on the other hand, one considers that the pressure is increased slowly and incrementally, the volumetric displacement of the liquid might follow a path similar to AC in Fig. 3. The work done in this case is given by the area ACD. This would be the reversible work. If we assume that the volumetric displacement changes proportionally to the increased pressure, the reversible work is one-half of the irreversible work of path ABC. Depending on the path chosen, the efficiency of work may vary. Thus, another variable η is introduced to account for the efficiency of work conversion.

Accordingly, we may equate the work performed by the arc force to the change in surface energy and potential energy of the liquid pool by the following:

$$\int_0^R G_2 dr = \int_0^R G_3 dr + \int_0^R G_4 dr \quad (3)$$

where $G_2 = \eta P_{arc} 2\pi r w$ and $\int_0^R G_2 dr$ is the fraction of work done by the arc force on the molten pool. The next term G_3 is given by:

$$G_3 = \sigma 2\pi r \left[1 + \left(\frac{dw}{dr} \right)^2 \right]^{1/2} - \sigma 2\pi r$$

where $\int_0^R G_3 dr$ is the difference between surface energy with surface depression

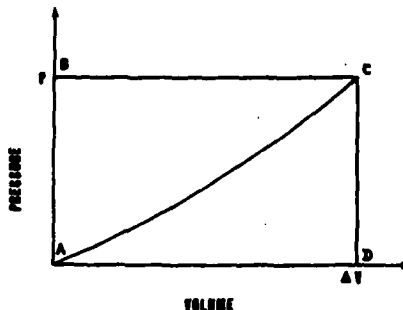


Fig. 3 - Reversible and irreversible $P\Delta V$ work. Reversible work is performed along path AC and irreversible work is performed along path ABC

and surface energy without surface depression of the molten pool, and finally

$$G_4 = \rho g 2\pi r (h - w) \left(H - \frac{h + w}{2} \right) -$$

$$\rho g 2\pi r h \left(H - \frac{h}{2} \right) = \rho g 2\pi r \left(\frac{w^2}{2} - wh \right)$$

where $\int_0^R G_4 dr$ is the difference between potential energy with surface depression and potential energy without surface depression of the molten pool.

Using equation (2), I can be simplified as:

$$I = \int_0^R \sigma 2\pi r \left[1 + \left(\frac{dw}{dr} \right)^2 \right]^{1/2} dr +$$

$$\int_0^R \rho g 2\pi r (Hh + \frac{w^2}{2} - \frac{h^2}{2}) dr$$

If we define

$$F = \sigma 2\pi r \left[1 + \left(\frac{dw}{dr} \right)^2 \right]^{1/2} +$$

$$\rho g 2\pi r (Hh + \frac{w^2}{2} - \frac{h^2}{2})$$

then $I = \int_0^R F dr$

Again using equation (2), equation (3) can be reduced to

$$\int_0^R G_2 dr = \int_0^R G_3 dr + \int_0^R G_5 dr$$

$$\text{where } G_5 = \rho g 2\pi r \frac{w^2}{2}.$$

We now define

$$G_6 = G_2 - G_3 - G_5 = \eta P_{arc} 2\pi r w -$$

$$\sigma 2\pi r \left[1 + \left(\frac{dw}{dr} \right)^2 \right]^{1/2} + \sigma 2\pi r - \rho g 2\pi r \frac{w^2}{2}$$

where $\int_0^R G_6 dr$ is the difference of work

performed by the arc force and the total system energy which is the summation of potential energy and surface energy.

If one applies the Euler-Lagrangian criterion (Ref. 12),

$$\frac{\partial}{\partial w} (F + \lambda_1 G_1 + \lambda_2 G_6) -$$

$$\frac{\partial}{\partial r} \frac{\partial}{\partial (dw/dr)} (F + \lambda_1 G_1 + \lambda_2 G_6) = 0$$

where λ_1 and λ_2 are Lagrange multipliers; one has a function which must be minimized subject to the two constraints noted previously.

After manipulation, the result of the Euler-Lagrangian criterion is

$$\frac{dt}{dr} = \frac{(1+t^2)^{1/2}}{\sigma r(1-\lambda_2)} \left[\rho g r w + \lambda_2 r (\eta P_{arc} - \rho g w) + \lambda_1 r - (1-\lambda_2) (1+t^2)^{-1/2} \cdot \left(\sigma t + \sigma t \frac{dw}{dr} - \sigma r \frac{t^2}{1+t^2} \right) \right] \quad (4)$$

if one sets

$$t = \frac{dw}{dr} \quad (5)$$

There are two boundary conditions
 $t = 0 \quad \text{at } r = 0$
 due to symmetry about the centerline of the weld pool and
 $w = 0 \quad \text{at } r = R$
 since the liquid must be in contact with the solid surface.

A computer program was developed to evaluate λ_1 and λ_2 . After evaluating λ_1 and λ_2 together with suitable boundary conditions and constraints, equations (4) and (5) are then solved simultaneously by the Runge-Kutta method (Ref. 13).

Parametric Analysis of the Model

In this model, there are five parameters which may be related to the welding process. These are:

1. The density of the molten metal, ρ .
2. The surface energy of the molten metal, σ .
3. The half width of the weld pool, R .
4. The arc pressure, P_{arc} .
5. The efficiency of work conversion, η .

The shape of the liquid-solid boundary is not included in this model. This is reasonable if movement of the gas-liquid boundary is small compared to the dimension of the weld pool. It may be argued from hydrostatics that the shape of the solid-liquid boundary will not influ-

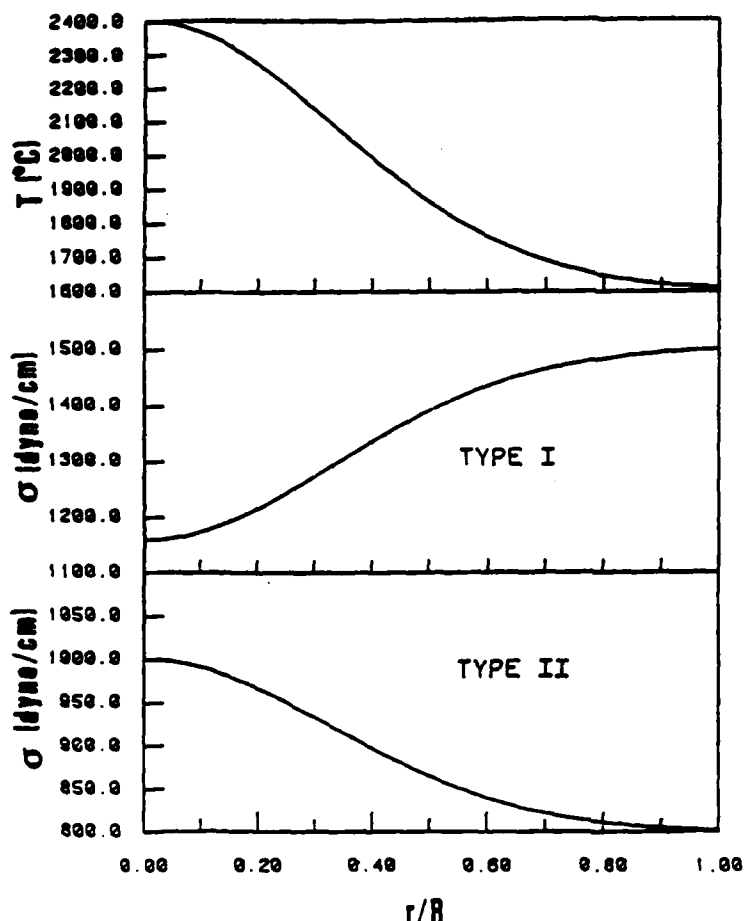


Fig. 4 - Assumed surface temperature and surface tension distribution of weld pool vs. reduced weld pool radius. Type I surface tension is believed to correspond to a steel without surface active elements while Type II surface tension is believed to represent a steel with surface active elements.

ence the result, provided the gas-liquid boundary does not impinge upon the solid-liquid boundary.

Steel and aluminum are chosen in this model with densities equal to 7.84 g/cm^3 and 2.7 g/cm^3 , respectively. For the distribution of surface energy of the molten pool, it is assumed that the temperature distribution on the top surface of the molten pool is as shown in Fig. 4A. The corresponding surface tension distributions are shown in Figs. 4B and 4C. Figure 4B is for pure iron, while Fig. 4C is for metal with high concentrations of surface active elements, e.g., sulfur and oxygen (Ref. 14).

The magnitude of these temperature and surface tension distributions are not appropriate for aluminum; however, the main purpose of choosing these distributions is to investigate the effect of surface tension on surface depression of a molten pool. Other results could be calculated for aluminum if accurate surface tension values were available. The half width of the weld pool is assumed to range from 0.5 to 1 cm (0.2 to 0.39 in.).

The arc pressure is taken from litera-

represent a physical reality, it may be sufficient to study the influence of arc pressure on surface depression of the weld pool.

Two values, 50 and 100%, are used to account for the efficiency of conversion of work done by the arc force to the change of surface energy and potential energy of the weld pool. The value of 100% corresponds to path ABC of Fig. 3, while the value of 50% corresponds approximately to path AC.

Results

The results of this model are shown in Figs. 6 to 11. A more complete set of tabulated results are listed in Table 1. The maximum depth of surface depression of the molten pool varies from 0.49 to 38.178 mm (0.019 to 1.504 in.); however, for reasonable pressures exerted by a 300 A arc, the maximum value is less than 1.3 mm (0.05 in.) for a 1 cm (0.39 in.) wide liquid steel pool. This is much less than the experimentally observed value of over 4 mm (0.16 in.)—Fig. 1.

Density of Molten Metal

When the density of molten metal increases, the surface depression depth is reduced as shown in Figs. 6 to 11. The effect of density becomes more prominent when the top surface of the weld pool becomes deeper. In Fig. 6, the maximum depth of surface depression for steel is 0.49 mm (0.019 in.) and for aluminum the maximum depth of surface depression is 0.642 mm (0.025 in.). Hence, reducing the density by nearly a factor of three increases the depression by only 30%. However, at higher arc pressures, as seen in Fig. 10, low density liquid has a maximum depth 160% larger than that of the heavy liquid.

Surface Tension

The effect of surface tension on the depth of surface depression of the weld pool is shown in Figs. 6 to 8. For the assumed surface tension distributions (types I and II as shown in Figs. 4B and 4C), the effect of surface tension on the shape of surface depression is not very important in both the low and the high surface depression ranges. The maximum surface depression depth is found to vary only 20% for the high density liquid and 40% for the low density liquid due to these different surface tension distributions.

Width of Weld Pool

The effect of weld pool width can be seen in Fig. 9 or by comparing Figs. 6 and 7. When the width of the weld pool increases, the surface depression depth also increases. As can be seen in Fig. 9,

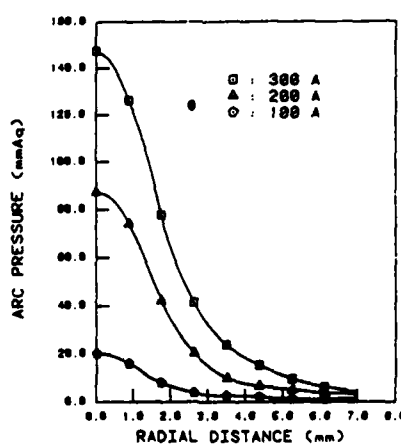


Fig. 5—Arc pressure distribution taken from literature (Ref. 2). Polarity—DCEN; electrode—4.0 mm (0.16 in.) diameter thoriated tungsten (90 deg); shielding gas—Ar; arc length—5 mm (0.197 in.)

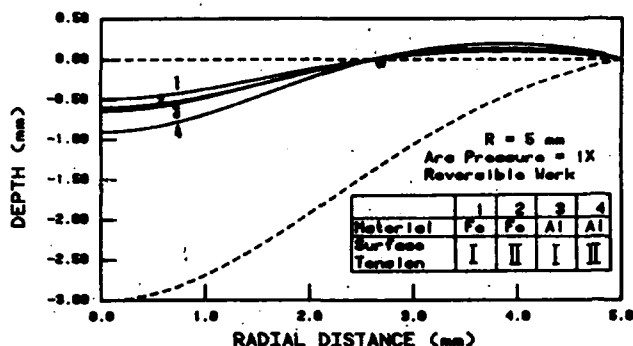


Fig. 6—Half surface depression curve at 300 A arc pressure assuming reversible work and a 1.0 cm (0.39 in.) wide weld pool. The dotted curve represents an approximate liquid-solid boundary

when the surface depression depth is small, the maximum depth increases only 80% when the weld pool width increases from 10 to 20 mm (0.39 to 0.79 in.). However, when the surface depression depth is large, the maximum depth increases 140% when the weld pool width increases from 10 to 20 mm (0.39 to 0.79 in.).

Arc Pressure

The arc pressure at 300 A causes a shallow depression (less than 2 mm, i.e., 0.078 in.). However, when the arc pres-

sure is very high, as shown in Figs. 10 and 11, the surface depression becomes very large. This may imply that at higher currents, the depth of surface depression is dominated by the strong arc pressure.

It should be noted that if the pressure distribution remains fixed in size, but increases parabolically with current, the pressures of 2, 4 and 6 times the measured pressure at 300 A would correspond to currents of 425, 600 and 735 A, respectively. If, on the other hand, the maximum pressure scales linearly with current, as has been confirmed in our laboratory (Ref. 15), these pressures

would correspond to 600, 1200 and 1800 A, respectively.

Work Conversion

The calculated depth of surface depression of irreversible work conversion is about two times larger than that of reversible work conversion, as shown in Figs. 9 and 11, which is not surprising.

Discussion

One of the more obvious criticisms of this model is the lack of a positive basis

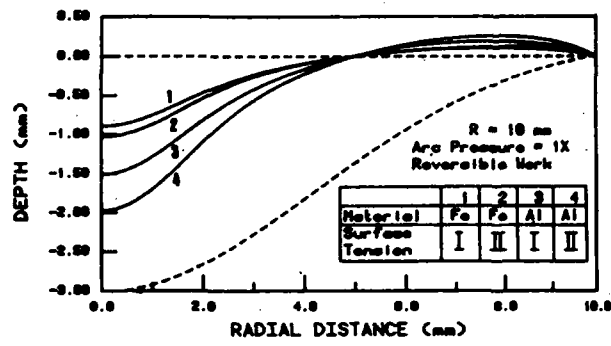


Fig. 7—Half surface depression curve at 300 A arc pressure assuming reversible work and a 2.0 cm (0.79 in.) wide weld pool. The dotted curve represents an approximate liquid-solid boundary

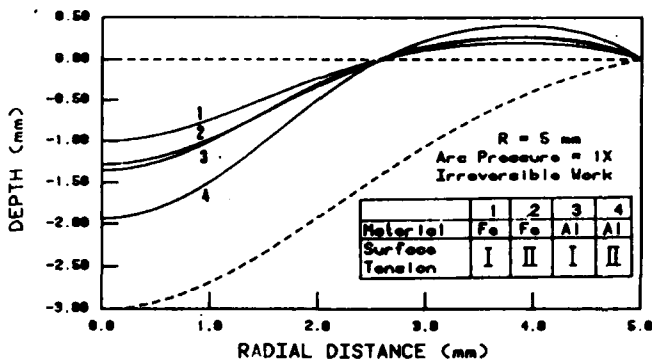


Fig. 8—Half surface depression curve at 300 A arc pressure assuming irreversible work. Compare with Fig. 6. The dotted curve represents an approximate liquid-solid boundary

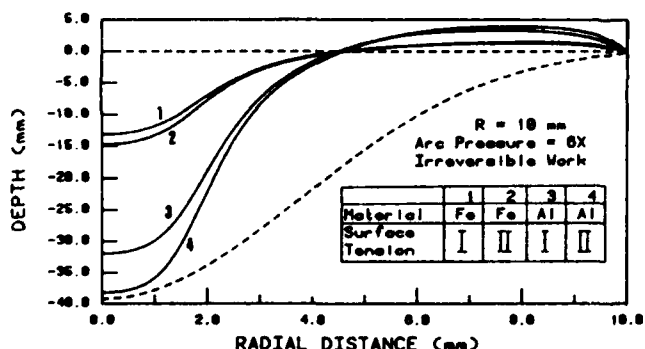


Fig. 10—Half surface depression curve at extreme arc pressure. The dotted curve represents an approximate liquid-solid boundary

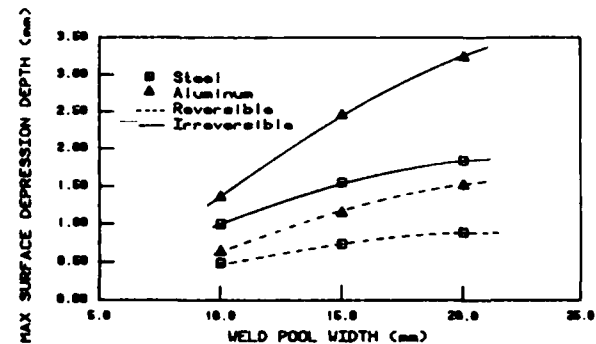


Fig. 9—Maximum surface depression depth vs. weld pool width for different materials and types of work conversion

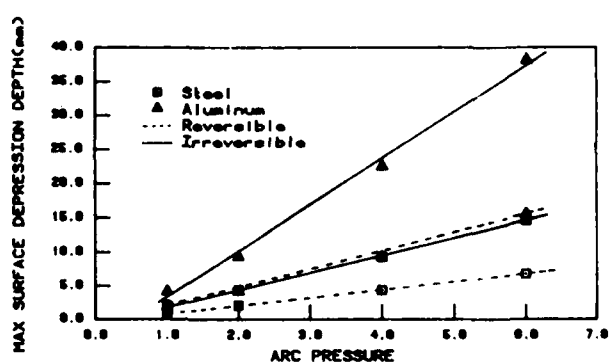


Fig. 11—Maximum surface depression depth versus arc pressure for different materials and types of work conversion. The numbers on the abscissa represent the multiplication factor of the arc pressure of the 300 A current in Fig. 5

Table 1—Calculated Maximum Depth of Surface Depression

Material	Half width, mm ^(a)	Arc pressure ^(b)	Surface tension	Work conversion	Max. depth of surface depression, mm ^(a)
Steel	5	1X	Type I	Rev.	0.490
Steel	5	1X	Type II	Rev.	0.600
Aluminum	5	1X	Type I	Rev.	0.642
Aluminum	5	1X	Type II	Rev.	0.903
Steel	10	1X	Type I	Rev.	0.893
Steel	10	1X	Type II	Rev.	1.029
Aluminum	10	1X	Type I	Rev.	1.511
Aluminum	10	1X	Type II	Rev.	1.975
Steel	5	1X	Type I	Irrev.	1.000
Steel	5	1X	Type II	Irrev.	1.282
Aluminum	5	1X	Type I	Irrev.	1.354
Aluminum	5	1X	Type II	Irrev.	1.938
Steel	10	1X	Type I	Irrev.	1.846
Steel	10	1X	Type II	Irrev.	2.127
Aluminum	10	1X	Type I	Irrev.	3.237
Aluminum	10	1X	Type II	Irrev.	4.210
Steel	5	2X	Type I	Rev.	1.000
Steel	5	2X	Type II	Rev.	1.279
Aluminum	5	2X	Type I	Rev.	1.354
Aluminum	5	2X	Type II	Rev.	1.938
Steel	10	2X	Type I	Rev.	1.857
Steel	10	2X	Type II	Rev.	2.132
Aluminum	10	2X	Type I	Rev.	3.235
Aluminum	10	2X	Type II	Rev.	4.212
Steel	10	6X	Type I	Irrev.	13.162
Steel	10	6X	Type II	Irrev.	14.731
Aluminum	10	6X	Type I	Irrev.	31.939
Aluminum	10	6X	Type II	Irrev.	38.178
Steel	5	2X	Type I	Irrev.	2.150
Steel	5	2X	Type II	Irrev.	2.712
Aluminum	5	2X	Type I	Irrev.	3.069
Aluminum	5	2X	Type II	Irrev.	4.650
Steel	10	6X	Type I	Rev.	6.821
Aluminum	10	6X	Type II	Rev.	15.572
Aluminum	5	4X	Type I	Rev.	4.641
Aluminum	10	4X	Type II	Rev.	9.372
Steel	7.5	1X	Type I	Rev.	0.741
Aluminum	7.5	1X	Type I	Rev.	1.142

^(a)25.4 mm = 1 in.^(b)This represents multiplication of the 300 A arc pressure data given in Fig. 5.

for selection of the work conversion efficiency, η . Although no direct rationale can be given for choosing either path ABC or path AC of Fig. 3, it is felt that path AC is more realistic. This is perhaps easiest to explain if one considers not the total depression from an initially flat metal surface to a fully depressed state; but rather, one might consider a small differential depression from an already depressed surface, due to minor arc pressure fluctuations. Such a restoration to a new equilibrium must follow path AC more closely than path ABC.

In addition, by viewing this system as a dynamic equilibrium where small changes in the arc force produce corresponding changes in the equilibrium surface shape, one can easily understand why other forms of energy (e.g., thermal energy) need not be considered to contribute to the formation of new surface area. Even if thermal energy were to create new surface area, the system must finally consume such new area as it is only the arc

force which balances the surface tension forces of the curved boundary. At final equilibrium, thermal energy cannot be considered to contribute to the balance of the arc force. Only other forces such as surface tension and hydrostatic forces can balance the arc force.

Finally, even if rather generous increases in arc force are postulated, it is seen that the experimentally observed surface depressions at 300 A cannot easily be explained by the arc force, no matter what the work conversion efficiency is assumed to be.

Experimentally, it has been observed that the surface depression at currents below 200 A is negligible. However, when current increases to about 300 A, a deep surface depression is found, as shown in Fig. 12. The maximum depth of surface depression is about 4.5 mm (0.18 in.) for stainless steel weld pools. From the model of the arc pressure, it is seen that the arc pressure cannot explain the deep surface depression at 300 A cur-



Fig. 12—Surface depression at 300 A of a stationary arc weld on Type 304 stainless steel: A—top surface during welding showing deep narrow depression; B—cross section of same weld. Note the porosity at the bottom of this finger indicating that the depression penetrated to the very bottom of the weld

rent, since the maximum depth of surface depression which was calculated for steel is 1.28 mm (0.050 in.). This is much smaller than the actual depth of surface depression which is experimentally found to be 4.5 mm (0.18 in.). Thus, some other mechanism must be responsible for the deep surface depression at these higher currents.

A simplified vortex model is proposed in this work to account for the deep surface depression at high currents. In this model, a compound vortex consisting of a forced vortex in the central part of the liquid pool with a free vortex surrounding the forced vortex is assumed.* This is shown schematically in Fig. 13. The result of the compound vortex model is shown in Fig. 14, assuming several angular velocities for the forced vortex. It can be seen that the depth of surface depression caused by the compound vortex can be close to the actual depth of the surface depression at high currents for angular velocities between 20 and 30 rad/s. Such circumferential flow can be seen in high

*A forced vortex is a region where the angular velocity ω_f is a constant. A free vortex is one that has constant angular momentum, i.e., $v_\theta = K/r$, where K is the vortex constant and θ is the azimuthal direction of cylindrical coordinates. The compound vortex matches a free vortex near the solid boundary with a forced vortex in the center of the weld pool.

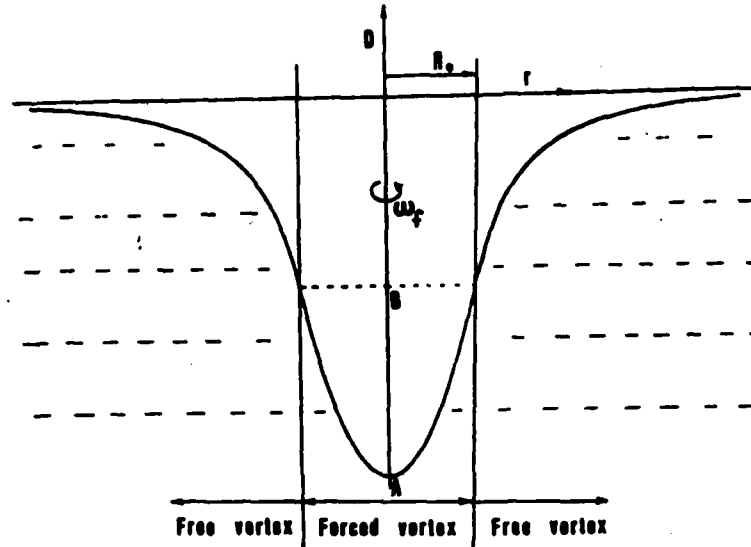


Fig. 13 - Structure of the compound vortex. Assuming no transition region between the forced and free vortex

speed movies of weld pools, which have oxide particles floating on the surface.

Flow, as that described above, may come from the toroidal flow on the plane parallel to the arc axis. Millere (Ref. 16) found that in electrically driven toroidal flow, a circumferential rotational motion on the plane normal to the arc axis is produced and increases with the intensity of electrovortex (toroidal flow) on the plane parallel to the arc axis. Therefore, part of the kinetic energy of toroidal flow on the plane parallel to the arc axis is transferred to circumferential motion, inducing flow on the plane normal to the arc axis.

It will be appreciated from Millere's work that such circumferential flow will not be strong if the system has perfect cylindrical symmetry. In real systems without perfect symmetry, the axial toroidal flow vector will be displaced from the

center line resulting in a circumferential velocity component which causes a circumferential precession of the toroidal flow into a helical shape. It should be noted that the maximum circumferential velocities assumed in Fig. 14 are less than one third of the velocities noted by Heiple and Roper (Ref. 17) using high speed cinematography; hence, these assumed rotational speeds are thought to be consistent with observed motion in actual weld pools.

As a result of this study, three current ranges may be proposed to explain surface depression of weld pools. At low currents (below about 200 A), the weld pool depression is shallow and does not significantly influence the shape of the weld pool. At higher currents (from about 300 to 500 A), the surface depression greatly influences the weld pool geometry. A circumferential vortex flow

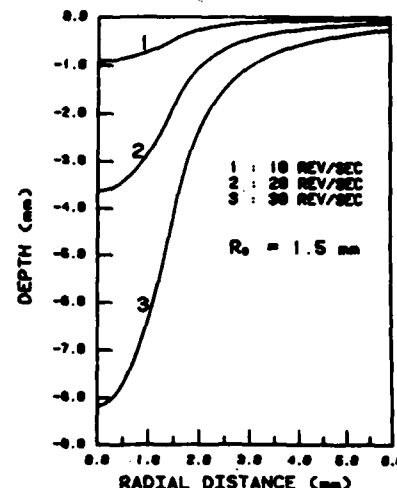


Fig. 14 - Depth induced by a compound vortex with a forced vortex region of 1.5 mm (0.06 in.) radius

may be responsible for the formation of this surface depression and the presence of the 'finger' penetration seen in gas tungsten arc spot welds, GMAW and SAW beads. At even higher currents (above about 500 A)*, the arc pressure is strong enough that it may explain some of the deep surface depression which, in turn, influences the weld pool geometry. The three current ranges proposed in this model are consistent with the results of Chihoski (Ref. 18) who found four distinct current ranges for the depth of penetration in aluminum welds. In his study, the penetration shows a very slow increase with current in the 100-200 A range, followed by a steep increase with current in the 200-300 A range. The 300-400 A range shows almost no response of current to penetration, but in the 450-600 A range, penetration begins to increase moderately with current.

Chihoski's 100-200 A range corresponds to the regime where surface depression is controlled by arc force and is not significant. The 200-300 A range corresponds to the transition from little surface depression to formation of a full vortex, while the 300-400 A range corresponds to bottoming out of the vortex depression at the solid boundary. In such a case, the current from the arc, or the heat, follows paths normal to the isopotential lines in the plasma and, hence, is concentrated at the top edges of the liquid vortex.

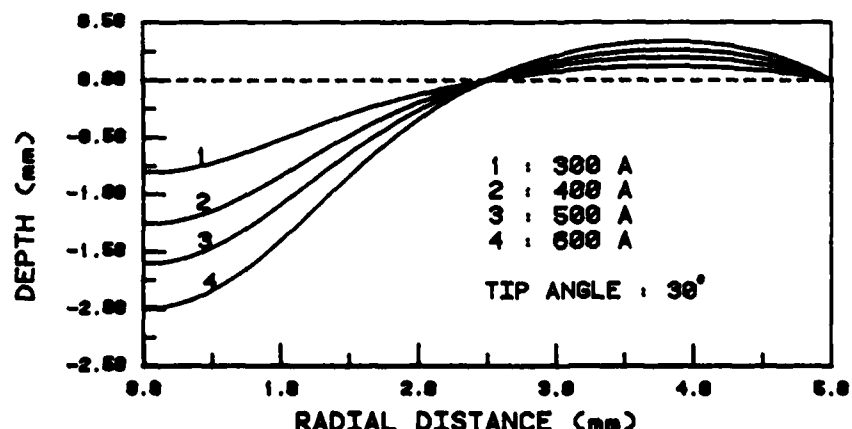


Fig. 15 - Half surface depression curve at different currents assuming reversible work. These surface depression curves are caused by the arc pressure measured in our laboratory

*More recent work by Lin and Eagar (Ref. 15) has shown that the depth of surface depression caused by the measured arc pressure at 600 A still cannot explain the deep crater of the weld pool found at even lower currents. Figure 15 shows the depth of the surface depression caused by the arc pressure measured in our laboratory.

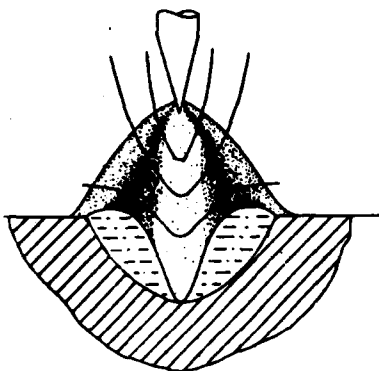


Fig. 16—Schematic representation of the equi-potential lines and the current density distribution when a deep crater forms. Note that the equi-potential lines around a deep depression suggest that the arc current (and hence the thermal energy) is distributed to the side walls of the pool and very little current (i.e., heat) reaches the bottom of the depression, as is depicted by the shaded region. Increased penetration due to the vortex formation is thus effectively stopped.

Conclusion

The depth of surface depression caused by the arc pressure distribution has been calculated using calculus of variations with suitable constraints. The results show that arc pressure only influences weld pool geometry at currents in excess of 500 A. At intermediate currents, the shape of the pool may be influenced markedly by circumferential convection. This flow may be responsible for the characteristic finger penetration of many weld pools. At even higher currents, arc force may become important and may have a significant influence on weld pool geometry.

Acknowledgments

The authors are grateful for support of this work by the Office of Naval Research under Contract N00014-C-80-0384. They also wish to thank the reviewers of this paper for their great care and many useful suggestions.

References

1. Selyanenkov, V. N., Stepanov, V. V., and Saifiev, R. Z. 1980. The dependence of the pressure of the welding arc on the parameters of tungsten electrodes. *Welding Production* 27(5): 6-8.
2. Unpublished technical support 1980. Osaka Transformer Co., Osaka, Japan
3. Shchetinina, V. I., et al. 1981. The dependence of the distribution of arc pressure on welding speed. *Welding Production* 28(4) 1-2.
4. Mazel', A. G., Yatsenko, V. P., and Rogova, E. M. 1977. On the force effect of the arc plasma flow on the weld pool. *Welding Production* 24(7): 5-8.
5. Stepanov, V. V., et al. 1977. Distribution of pressure in the plasma arc, and effects of the rate of flow of plasma-forming gas on weld quality. *Auto. Weld.* 30(6): 5-7.
6. Yamauchi, N., et al. 1980. Development and application of high TIG process-SHOTTA welding process. *Proceedings of International Conference on Welding Research in the 1980's*, Osaka, October, 1980, pp 25-30.
7. Savage, W. F., Nippes, E. F. and Agusa, K. 1979. Effect of arc force on defect formation in GTA welding. *Welding Journal* 58(7): 212-s to 224-s
8. Ishizaki, K. 1980. A new approach to the mechanism of penetration. *Weld Pool Chemistry and Metallurgy*, pp 65-70. The Welding Institute International Conference, London, April, 1980.
9. Friedman, E. 1978. Analysis of weld puddle distortion and its effect on penetration. *Welding Journal* 56(6) 161-s and 166-s
10. Lin, M. L., and Eagar, T. W. 1983. Influence of surface depression and convection on arc weld pool geometry. *Transport Phenomena in Materials Processing*. ASME PED-Vol 10, November 1983, pp 63-69.
11. Burleigh, T. D. and Eagar, T. W. 1983. Measurements of the force exerted by a welding arc. *Met. Trans* 14A(6): 1223-1224
12. Ketter, R. L., and Prawel, S. P., Jr. 1969. *Modern methods of engineering computation*. New York: McGraw-Hill.
13. Milne, W. E. 1962. *Numerical solution of differential equation*. New York: John Wiley & Sons.
14. Keene, B. J., et al. 1982. Effects of interaction between surface active elements on the surface tension of iron. *Canadian Metallurgical Quarterly* 21(4): 393-403.
15. Lin, M. L., and Eagar, T. W. Unpublished work.
16. Millere, R. P., et al. 1980. Effect of a longitudinal magnetic field on electrically driven rotational flow in a cylindrical vessel. *Magnetohydrodynamics* 16(1): 66-69.
17. Heiple, C. R., Roper, J. R., Stagner, R. T., and Aden, R. J. 1983. Surface active element effects on the shape of GTA, laser and electron beam welds. *Welding Journal* 62(3): 72-s to 77-s
18. Chishaku, R. A. 1970. The rationing of power between the gas tungsten arc and electric arc. *Welding Journal* 49(2): 64-s to 82-s

Appendix

Referring to Fig. 13, the depth produced by a compound vortex may be estimated as follows.

In the forced vortex region ($r \leq R_0$), the angular velocity is constant and

$$D_1 = \frac{\omega_1^2 r^2}{2g}$$

with the origin referred to point A in Fig. 13.

In the free vortex region ($r > R_0$), the angular momentum is constant and

$$D_2 = \frac{\omega_1^2 R_0^4}{2g} \left(\frac{1}{R_0^2} - \frac{1}{r^2} \right)$$

with the origin referred to point B in Fig. 13. The total depression $D = D_1 + D_2$.

List of Symbols

T—temperature on the surface of weld pool (°C)
 J—total system energy(erg)
 σ—surface energy(erg/cm²)
 ρ—density of liquid metal(g/cm³)
 g—gravitational acceleration(cm/s²)
 h—ordinate of solid-liquid boundary(cm)
 w—ordinate of liquid-gas boundary(cm)
 r—radial coordinate of weld pool(cm)
 H—maximum depth of liquid pool(cm)
 R—radius of the top surface of liquid pool(cm)
 η—percentage of work conversion(%)
 D—depth of liquid pool produced by a compound vortex(cm)
 R₀—radius of forced vortex region(cm)
 ω₁—angular velocity of rotational motion in forced vortex region(rad/s)

As such, direct arc heat does not reach the bottom of the vortex, as shown in Fig. 16. Hence, no further melting occurs at the bottom of the depression and no further penetration results. Above 450 A, the arc pressure becomes significant and, together with the vortex, deepens the depression as the current is increased.

Although the analytical arc force model presented here applies only to partial joint penetration welds,* it is believed that the vortex model is applicable to both complete and partial joint penetration beads. However, more study of the strength and mechanism of vortex formation is needed to confirm this hypothesis. Finally, it should be noted that if arc force were in fact the dominant cause of surface depression in welding, the depression would change markedly with changes in liquid density.

When a vortex is considered the cause of surface depression, there is no dependence of depression on density. The fact that finger penetrations in aluminum and steel are of nearly equal depth is considered supportive of the vortex model. In addition, the experimental shape of finger penetration, as seen in Fig. 12B, is thought to be more consistent with a vortex model than an arc force model.

*For an analysis of arc force on full penetration welds, see Friedman (Ref. 9).

END

FILMED

10-85

DTIC